ANNALS OF GEOPHYSICS, 67, 6, S661, 2024; doi:10.4401/ag-9124
OPEN ACCESS

A state-of-the-art analysis system designed to monitor microseismicity at a local scale

Andrea Morelli[*,1], Mario Anselmi[2], Thomas Braun[3], Stefania Danesi[1], Maddalena Errico[1], Daniela Famiani[3], Alexander Garcia[1], Irene Molinari[1], Maurizio Vassallo[3], Lucia Zaccarelli[1], Giampaolo Zerbinato[1]

(1) Istituto Nazionale di Geofisica e Vulcanologia, Sezione di Bologna, Bologna, Italy
(2) Istituto Nazionale di Geofisica e Vulcanologia, Osservatorio Nazionale Terremoti, Roma, Italy
(3) Istituto Nazionale di Geofisica e Vulcanologia, Sezione Roma 1, Roma, Italy

Article history: July 10, 2024; accepted February 18, 2025

Abstract

In this paper, we review the procedures involved in establishing a contemporary workflow for real-time microseismic monitoring using a local-scale seismographic network. We draw on our specific experience in monitoring potentially induced or triggered seismicity at two adjacent oil extraction sites in the Basilicata region of Southern Italy. This monitoring effort is conducted within a regulatory framework that adheres to established guidelines. However, we perceive our undertaking as generally appropriate for any local-scale seismographic network, irrespective of the specific application planned. For this reason, here we limit ourselves to discussing issues related to accurate detection, location, and quantification of microearthquakes as discrimination of their causative process is beyond the scope of this paper. We provide an overview of the tools and methodologies essential for effective monitoring, as well as the necessary approaches for assessing the reliability and accuracy of results, with the aim of offering practical guidance to those undertaking similar projects. The paper outlines the acquisition and analysis systems, including both hardware and software components, that we routinely deploy. We assessed the spatial variability of the detection threshold of the network employing an approach based on the comparison of the actual noise level recorded at the seismic stations with the theoretical spectra corresponding to the rupture models for small earthquakes. Furthermore, various tests were conducted to ascertain the significance of noise levels and hypocentral depths on the computed detection thresholds. Special attention is given to the critical issue of addressing the inherent uncertainties in the determination of hypocenters, a factor often underappreciated in such operations. While many advanced tools are available to network operators, optimal results require proper configuration and rigorous testing of these systems.

Keywords: Seismographic networks; Microseismicity; Earthquake detection; Earthquake location; Seismic noise; Seismic monitoring

1. Introduction

For decades, seismic networks – comprising multiple digital seismographs distributed across a designated area of interest, with centralized, continuous data acquisition and real-time analysis – have been utilized to monitor seismic activity at various scales. These networks range from global (e.g., Oliver and Murphy, 1971; Romanowicz et al., 1984; Butler et al., 2004; Ringler et al., 2022), to regional (e.g., Boschi et al., 1991; Liu et al., 2008; Hetényi et al., 2018; Margheriti et al., 2021), and local scales (e.g., Priolo et al., 2015; Nolte et al., 2022). In some cases, they are even employed to monitor the dynamic behavior of individual structures (e.g., Snieder and Şafak, 2006; Morelli et al., 2021). Local seismic networks are frequently designed to detect and analyze microseismicity (e.g., Chiaraluce et al., 2009; Bianchi et al., 2015; Anselmi et al., 2020 among many others), characterized by very small, often negative magnitude events. Such events are of particular interest when they are potentially linked to anthropogenic activities, particularly in contexts involving the exploitation of subsurface natural resources (i.e., induced seismicity, e.g., Ellsworth, 2013; Grigoli et al., 2017; Braun et al., 2018a).

Although the origins of modern seismography can be traced back slightly earlier (see, e.g., the references in Dziewonski, 1994), the 1990s marked a truly transformative period for the field. This decade saw the widespread adoption of force-balanced (very-) broadband seismographs (Wielandt and Steim, 1986), the establishment of modern network operations driven by (near-) real-time data transfer and analysis, and the emergence of extensive collaboration frameworks among operators. Prominent initiatives during this period include the Federation of Digital Seismograph Networks (Dziewonski, 1994; Jepsen, 1994; North, 1994; Chen et al., 1994; Roult and Montagner, 1994; Hanka and Kind, 1994; Boschi and Morelli, 1994; Butler, 1994), ORFEUS in Europe (Dost, 1994), and the IRIS initiative in the United States (Ahern, 1994). A pivotal development during this time was the establishment of a new Standard for the Exchange of Earthquake Data (Ahern et al., 2009), which emerged from extensive community discussions and was subsequently widely adopted. It is fair to assert that modern seismic network operations today are deeply rooted in the standards and procedures that originated during the 1990s. While global cooperation and data exchange among seismological institutions have been in place since the early 20th century – notably through the International Seismological Centre (e.g., Rothé, 1981) – this cooperation was primarily focused on sharing parametric data resulting from the processing of arrival times. However, the 1990s represent a significant turning point, marking the birth of what can be recognized as modern seismography.

Extensive experience in the design and operation of seismic networks has led to the accumulation of substantial knowledge and the development of numerous well-tested tools, many of which are publicly accessible and freely shared within the scientific community. However, establishing new seismic network operations from scratch, particularly in a continuous and near-real time operational mode, remains an elaborate and time-consuming process, often requiring multiple iterations and trial-and-error adjustments. Numerous critical decisions must be made, and considerable effort is required to configure and test the entire analysis workflow. In this paper, we provide a detailed account of our recent experience, aiming to review the decision-making process, implementation strategies, and system configuration in a manner that is both broadly informative and – hopefully – practically useful to others undertaking similar initiatives. In many respects, this paper represents the resource we wish had been available when we first confronted these challenges.

A prime application for a local seismograph network is to monitor crustal microseismicity possibly involved with underground energy technologies. It is well known that anthropogenic activities interacting with crustal rocks – such as mining, fluid extraction or injection, and water impoundment in reservoirs – can modify the stress state of the rocks and potentially induce earthquakes (e.g., Grigoli et al., 2017). In active tectonic regions, even relatively minor stress changes from industrial activities can trigger the failure of a fault already near its critical stress (e.g., Dahm et al., 2013). In other cases, hydraulic fracturing has caused earthquakes in previously aseismic regions (e.g., Ellsworth, 2013). In all scenarios, induced or triggered earthquakes that may impact populations and property are undesirable. Efforts to manage and mitigate the risks associated with the use of underground natural resources are driven by the need to protect both the natural and built environments, as well as human populations and workforces. As demand for energy and mineral resources increases and urbanization expands, concerns about the impact of these industrial activities continue to grow. In response to the rising awareness of risks from anthropogenic seismicity, many countries have implemented control protocols for systematically monitoring seismicity, ground deformation, and fluid pore pressure to reduce the potential impact of industrial activities. These protocols often employ a Traffic Light System (TLS), which dictates the reduction or even cessation of industrial operations when control parameters exceed certain thresholds (Bommer et al., 2006; Grigoli et al., 2017;

Baisch et al., 2019; Braun et al., 2020). Such systems require observations from local seismic networks and reliable near-real time analysis. Although a detailed discussion of the effectiveness of TLS for mitigating induced or triggered seismicity is beyond the scope of this paper, it is helpful to briefly introduce the operational framework. The system described here serves as a prime example of one of the possible applications of a local seismic network.

Although Traffic Light Systems (TLSs), which rely on the exceedance of fixed threshold values, are widely used in various operational environments, Baisch et al. (2019) have highlighted significant limitations in their predictive capabilities. These limitations arise primarily from the assumptions inherent in the conceptual models of seismic nucleation and evolution. As a result, they recommend designing TLS protocols tailored to each specific operational environment, using geo-mechanical models and changes in the stress field as indicators of the robustness of the monitoring system. Earthquake magnitude is the most commonly used parameter for defining TLS warning thresholds. Along with peak ground velocity (PGV) and peak ground acceleration (PGA), it contributes to TLS design in accordance with the current Italian guidelines for monitoring hydrocarbon extraction activities (Indirizzi e Linee Guida per il monitoraggio, ILG; Dialuce et al., 2014). Interestingly, Schultz et al. (2021) proposed a risk-informed approach for setting maximum alert thresholds, which takes into account both damage levels and nuisance to the population. This approach builds TLS parameters using geographically variable iso-risk maps. High-quality microseismic monitoring remains a crucial tool for providing near-real time evaluations of rapidly changing conditions, often influenced by human activity. It enables data-driven decisions through adaptive and objective assessments. While distinguishing between anthropogenic and natural seismicity in real or near-real time remains a significant challenge (e.g., Dahm et al., 2013; Goebel et al., 2015), microseismic monitoring enhances our understanding of how the crust responds to stress perturbations caused by human activities. By quantifying changes in seismicity rates, it can help identify possible fluid migration or define spatial patterns of rupture nucleation.

Several methods exist to estimate the initiation point and origin time of an earthquake rupture (e.g., Havskov et al., 2002). The most prevalent method involves determining the origin point from where seismic waves propagate, assuming a known wave speed, to a network of seismographs (e.g., Karasözen and Karasözen, 2020). To detect an earthquake, the initial step is to identify the arrival of energy at each individual sensor, known as *detection*. Subsequently, it is necessary to ascertain whether certain arrivals at different stations exhibit coherence, given a known wave propagation speed and a single potential source (phase *association* to create an *event*). Once the event is confirmed, energy arrivals are timed (*arrival time pick*), and the origin time and location (*hypocenter*) are estimated. The intent to detect feeble small-magnitude events, and the contributions to ground motion originating from natural and anthropogenic sources (such as wind, sea waves, road traffic, machinery, etc.) generally referred to as *ambient noise*, require some careful parameter tuning to local conditions to reach the best performance. The classical and most common method to detect the arrival of energy is based on the amplitude ratio of a short-term average of the amplitude of incoming signal versus a long-term average (this is known as *STA/LTA*, e.g. Trnkoczy, 2002). Other methods have been proposed that take advantage of waveform shapes. Matched filtering involves cross-correlating recorded seismic data with known event templates to identify similar patterns (e.g., Shearer, 1994). This technique enhances the detection of low magnitude microseismic events that may be obscured by noise. Advanced deep learning models have also been developed to detect microseismic events (e.g., Zhu and Beroza, 2019). These models leverage neural networks to automatically identify and characterize seismic events, improving detection accuracy and efficiency. Full waveforms contain more information than arrival times only, and their use for location (also using reverse-time source imaging) and classification is receiving increasing interest (see e.g. the review by Cesca and Grigoli, 2015).

Microseismic monitoring largely relies on traditional seismological methods that must be carefully adapted to meet the specific needs of this application. Key elements include configuring the seismic network appropriately, setting up automatic detection and processing systems, and implementing effective post-processing routines – all of which are essential for the successful routine monitoring of underground operations. Detection and location methods typically fall under two primary approaches: arrival time pick and waveform-based. The more traditional pick-based methods encompass phase detection and identification, event association, and location refinement. Phase detection entails identifying alterations in waveform energy, frequency content, or polarization, which correspond to seismic phase arrivals (e.g. Grigoli et al., 2018). Automated phase picking is standard for the initial arrivals of P and S waves. Here, we present our ongoing experience in utilizing various seismic networks to meet the objectives and performance standards prescribed by regulatory policies (Dialuce et al., 2014). Due to the necessity of well-established and rigorously tested procedures that are essential for fiduciary routines, we adhere to the

more conventional approach based on the arrival phase selection. We assess the impact on overall monitoring performance by integrating data from specific networks with available open-access seismographic stations (from both national and local initiatives), evaluating detection thresholds based on background noise. Automatic detection algorithms must be finely tuned to accommodate the resulting heterogeneous and integrated network.

In this paper, we focus exclusively on the analysis of data generated by an existing seismic network, without addressing the challenges associated with planning and deploying instrumentation in the field. The design and implementation of a seismological instrument array involve numerous factors, such as array geometry, hardware selection, site location (considering exposure to natural and anthropogenic noise, accessibility, and proximity to power and communication infrastructure), and sensor placement (e.g., Bormann, 2012; Nolte et al., 2022). Our objective here, however, is to review and document the decisions necessary for establishing a near-real time data analysis system for a local seismic network, specifically aimed at monitoring potentially induced seismic events. While our case is particular, the principles and considerations outlined apply broadly to any local network designed to monitor low-magnitude seismicity, whether on a volcanic structure, within industrial settings, or overactive tectonic regions. The paper begins by outlining the primary objectives of the seismographic network and providing a concise description of the geological context, which is crucial for interpreting the results. We then detail the data acquisition and analysis system, categorizing various sources of noise and disturbances and discussing their effects on network performance and the calibration of automatic detection algorithms. Additionally, we describe adaptations to the seismological analysis workflow in response to specific environmental conditions, such as the selection of an appropriate local magnitude scale. Finally, we conclude with a discussion on the importance of implementing realistic estimates of uncertainty in seismic event determinations.

2. The High Agri River and Sauro Stream valleys, Southern Italy: geologic setting and instrumental network

A comprehensive understanding of the seismotectonic background is essential for analyzing local seismicity in any region, making a preliminary review of relevant literature advisable. Accordingly, we provide a concise overview of the geological and tectonic setting of the area under study. The southern Apennines form part of the NW-SE oriented Apennine thrust-and-fold belt (Fig. 1), which is undergoing a general NE-SW extensional regime. This belt is bounded to the east by a Plio-Pleistocene foredeep and to the west by the Tyrrhenian back-arc basin (Malinverno and Ryan, 1986; Casnedi et al., 1988). The compressional belt evolved through two distinct tectonic phases with differing styles: (1) an initial Neogene thin-skinned phase, involving thrust sheets composed of Meso-Cenozoic sedimentary units from the internal Apennine Platform and Lagonegro Basin, along with associated foredeep flysch deposits, which were thrust over the Inner Apulian Platform; and (2) a subsequent Late Pliocene-Early Pleistocene thick-skinned phase, during which deeply-rooted, high-angle N- to NW-trending thrusts with antithetic back thrusts generated long-wavelength anticlines within the Apulian platform (Menardi Noghera and Rea, 2000; Mazzoli et al., 2001; Shiner et al., 2004). It remains unclear from the existing literature whether these deformation styles operated simultaneously, contributing to the formation of both foredeep and piggyback basins. The Apulian platform consists of a 6 ÷ 8 km thick succession of Meso-Cenozoic shallow-water carbonates, with anticlines in these carbonates serving as the primary traps for oilfields, sealed by Pliocene siliciclastic foredeep deposits.

The upper Agri River valley (hereafter referred to as Val d'Agri; Fig. 2) is a Quaternary extensional basin formed by two active, high-angle, range-bounding fault systems with opposing dips: the Monti della Maddalena Fault System (MMFS) and the Eastern Agri Fault System (EAFS) (Cello et al., 2003; Maschio et al., 2005). Significant normal-faulting earthquakes have occurred along the axial sector of the southern Apennines, impacting the Val d'Agri area. The most recent of these was the M7 earthquake of 1857. Although the identity of the causative fault remains debated, recent studies have linked the 1857 event to a segment of the Monti della Maddalena Fault System (Burrato and Valensise, 2008; López-Comino et al., 2021).

The Tempa Rossa-Gorgoglione valley, traversed by the Sauro Stream (Fig. 2), is a piggyback basin where thick Miocene and Plio-Pleistocene foredeep units, thrust over the Apulian Internal platform, are exposed within the belt's external domains. Beneath this basin, the Apulian Internal platform is characterized by compressive structures, such as the Tempa Rossa structure, and exhibits thrusting over the Apulian External platform. The latter, however, is influenced by extensional structures, attributed to flexural processes during under-thrusting (Menardi Noguera and Rea, 2000; Bertello et al., 2010; López-Comino et al., 2021).

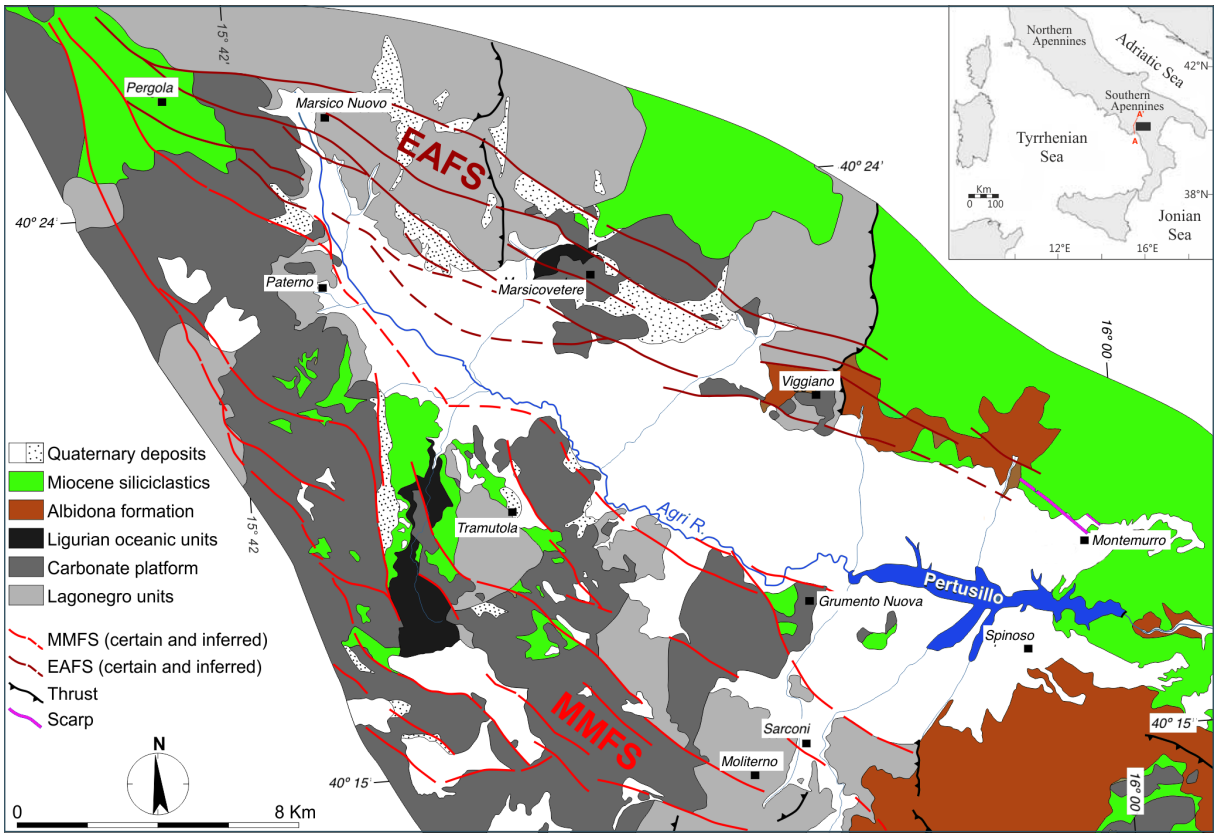

Figure 1. Schematic geological map of the High Agri Valley in the Italian Southern Apennines (modified after Giocoli et al., 2015). Downloaded from https://commons.wikimedia.org/wiki/File:Schematic-geological-map-of-the-High-Agri-Valley.png on June 20th, 2024; licensed under Creative Commons Attribution 3.0 Unported License. Inset at top right shows with a black box the location of the detailed map in the main figure in a regional setting, and – with a red line – the approximate location of the cross section shown in Fig. 2. MMFS: Monti della Maddalena Fault System; EAFS: East Agri Fault System.

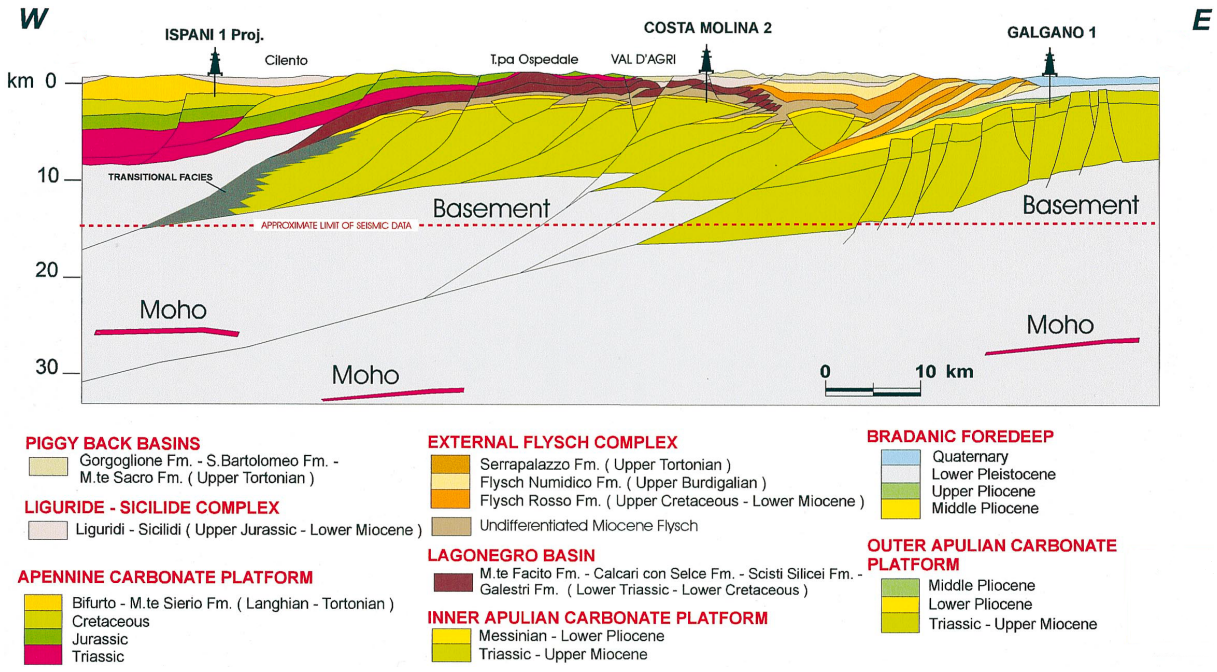

Figure 2. Structural cross section across the Val d'Agri and Tempa Rossa extensional basins (for approximate location see inset map in Fig. 1; modified after Menardi Noguera and Rea, 2000).

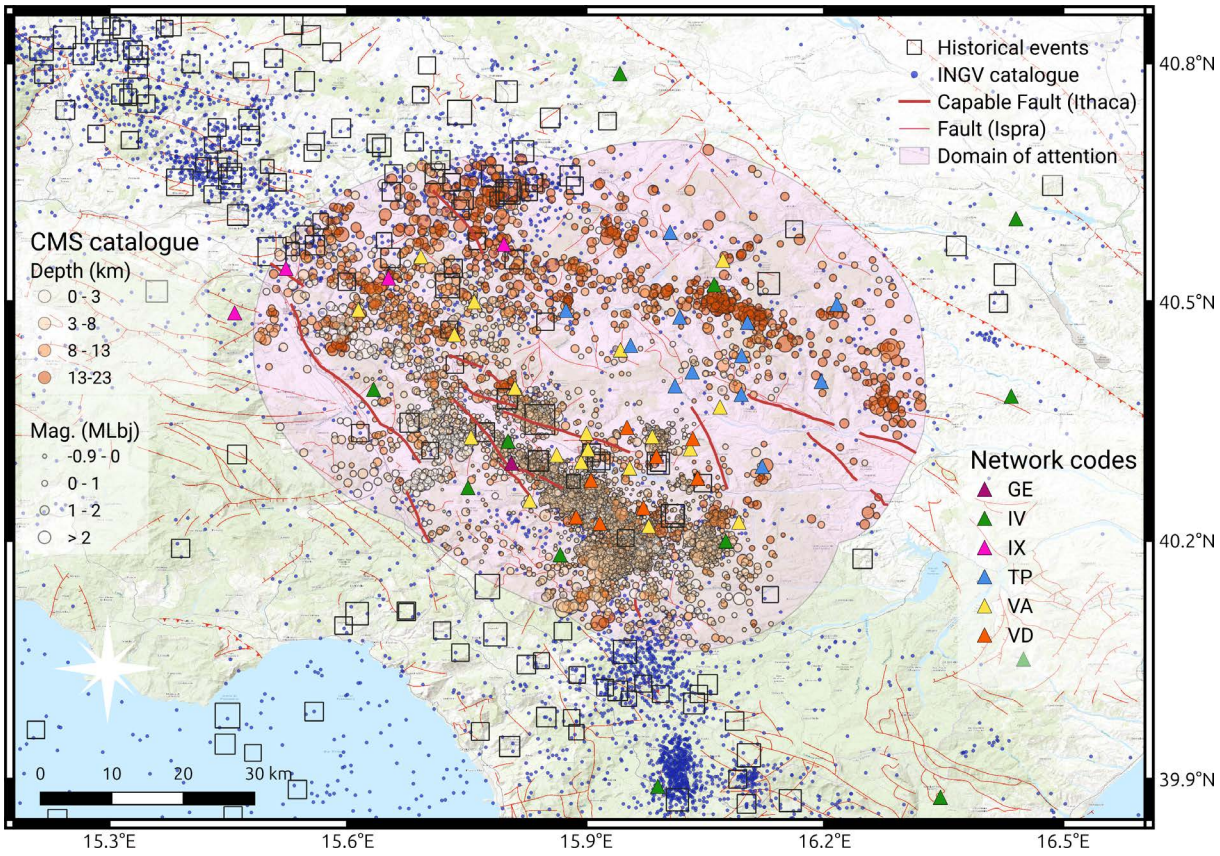

Figure 3. The integrated seismographic network in the Val d'Agri and Gorgoglione region, subject to analysis. Triangles represent seismographic stations, shown in different colors to mark the different networks (as shown in legend). The light-pink shaded area represents the Domain of Interest (DI) for the integrated network. The CMS catalog from analysis of the integrated network only covers this DI. Epicenters are shown with circles colored by depth classes and sized according to magnitude, see legend. Capable fault traces (thick red lines) are from ITHACA Working Group (2019). Thin red lines show other tectonic lineaments from ISPRA (2025). Historical earthquakes (open squares) are taken from the CPTI15 catalog (Rovida et al., 2022). Background instrumental seismicity is taken from from the INGV catalogue (ISIDe Working Group, 2007).

This area is seat of diffused low-magnitude seismicity (Fig. 3). Valoroso et al. (2009) have shown that seismic activity, occurring mostly in spring after loading of artificial Pertusillo Lake, suggests reservoir-induced seismicity triggered by fluid pressure diffusion (Valoroso et al., 2009). Wastewater injection into the Val d'Agri oil field has also been shown by Improta et al. (2017) to induce microseismicity. That study suggests that injection pressure is the primary driver of seismicity, channeling through a high-permeability fault damage zone.

In this region, two significant oil reservoirs are under exploitation through separate concessions: the Val d'Agri reservoir, the largest onshore oil reservoir in Europe, and the adjacent Gorgoglione-Tempa Rossa reservoir. Through an agreement between the regional government of Basilicata (Regione Basilicata, RB) and the relevant national authority (initially under the Ministry of Economic Development, MiSE, now under the Ministry of Environment and Energy Security, MASE), the Istituto Nazionale di Geofisica e Vulcanologia (INGV) is responsible for monitoring microseismicity and ground deformation, following the guidelines outlined in Section 2 (ILG, Dialuce et al., 2014; see also Braun et al., 2020).

Instrumental networks for geophysical monitoring in the field are managed by the industrial operators. Numerous seismic stations, administered by these operators and deemed both numerically and qualitatively adequate to meet the prescribed monitoring requirements, are distributed across the Val d'Agri and Gorgoglione areas. The Val d'Agri seismograph network (network code VA) has been operated by ENI SpA since 2001, starting with initial installations that have since expanded and been modernized. Currently, the network comprises 20 stations. In line with the ILG guidelines (Dialuce et al., 2014), substantial upgrades have been made to improve

infrastructure and achieve the required performance, including new installations. Stations previously operating in triggered mode have been upgraded to ILG standards with 24-bit digitizers, continuous acquisition at a 200 Hz sampling rate, and real-time data telemetry. In the Gorgoglione area, Total E&P Italia S.p.A. manages a newly installed network (network code TP) of 12 seismic stations designed in accordance with regulatory guidelines for microseismic monitoring (TOTAL E&P Italia Spa, 2018). Each station is equipped with both an accelerometer and a velocimeter, acquiring continuous data at a 200 Hz sampling rate in real time. Technical specifications for all sensors, digitizers, velocimeters, and accelerometers across both networks are recorded in the IRIS Nominal Response Library (NRL) database (http://ds.iris.edu/ds/nrl/, last accessed: July 10, 2024). In addition to the Val d'Agri and Gorgoglione networks, data acquisition is extended to select stations from other public networks: IV (INGV, 2005), VD (CNR IMAA, 2019), IX (Irpinia Seismic Network – ISNet, 2005), and GE (GEOFON Data Centre, 1993). Network integration may significantly enhance microseismic monitoring by improving network geometry and spatial coverage. The complete integrated virtual network across the Basilicata region consists of 56 seismic stations (Fig. 3). The stations within these networks operate in locations with widely varying noise characteristics. For example, IV stations, installed to monitor Italian seismicity in free-field conditions, are often located away from urban centers and experience low noise levels. In contrast, the VA and TP stations in the Val d'Agri and Gorgoglione oilfields generally have higher noise levels for periods under one second – unfortunately, the primary range for monitoring small-magnitude seismicity – due to industrial activities, as discussed in a later section. Incorporating open stations available in the region introduces heterogeneity in terms of instrument response (largely addressed by standardized FDSN metadata) and site noise characteristics. However, it also significantly enhances the spatial coverage of the network and it is quite common practice. When feasible, this approach is highly recommended, as the advantages of expanded coverage and data richness generally outweigh the added technical challenges.

3. Data acquisition and analysis

In designing the computing hardware and software infrastructure for a seismic monitoring system, it is essential to consider key performance requirements. For our implementation, the primary mission-critical needs to ensure reliable, near real-time data acquisition and analysis include robust IT security; data protection for stations with restricted access; and system failure tolerance via redundancy in processing routines and data storage (both raw and processed). To meet these requirements, we implemented a redundant hardware infrastructure (Fig. 4) comprising two independent servers and a storage array. An additional layer of disaster recovery is provided by mirroring a data buffer onto a virtual machine hosted in a separate institutional data center in Rome.

For data acquisition and analysis, two identical physical servers were selected, each hosting two virtual machines that operate concurrently and independently. Each server includes one virtual machine dedicated to real-time data acquisition and another that manages automatic data processing, data storage, and post-processing by analysts. This modular design supports fault tolerance: in the event of a failure in one physical server, the other can continue uninterrupted data acquisition and processing.

Each server is equipped with a 40-core Xeon CPU configured for hyper-threading and 4 TB of RAM. The four virtual machines are allocated 8 cores and 20 GB of RAM each, run on the Linux Centos 8 operating system, and use SeisComP for data acquisition and processing [Seiscomp, https://www.seiscomp.de/, last accessed July 10, 2024]. Real-time seismic data acquisition relies on a Common Acquisition Protocol Server (CAPS) module [CAPS, https://docs.gempa.de/caps/current/base/introduction.html, last accessed July 10, 2024]. Seismological data, databases, and virtual machine volumes are stored on a Dell SCV-3000 storage array. A simplified configuration diagram is provided in Fig. 4.

The acquisition and processing software is installed on two virtual machines (Fig. 4). The *Acquisition 1 VM* is dedicated to acquiring and storing seismological data from the seismic stations, with data archived by the CAPS server. The *Processing & DB 1 VM* then processes this data, made available by the *Acquisition 1 VM*, both of which run on the same physical hardware unit (Hypervisor 1). Each virtual machine operates on the Centos 8 system and is supported by two volumes in the storage array: one for the operating system and another for data. Both virtual machines are implemented via libvirt [Libvirt, https://libvirt.org, last accessed on July 10, 2024] on a Debian 10 operating system hosted by Hypervisor 1. Device mapper multipath [Device Mapper Multipathing, https://access.redhat.com/documentation/it-it/red_hat_enterprise_linux/6/html/dm_multipath/mpio_overview, last accessed on July 10, 2024] enables the connection between the hypervisor and the storage array (Fig. 4).

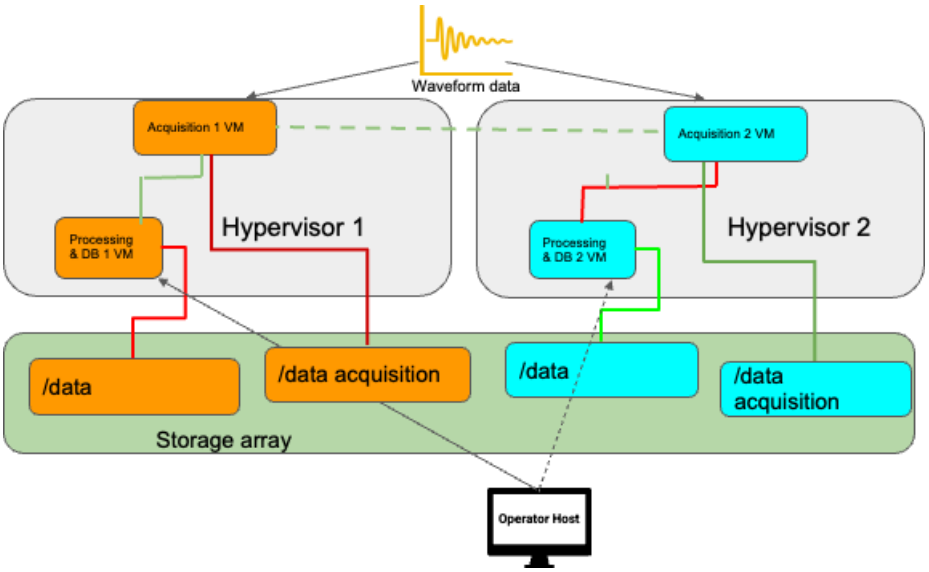

Figure 4. Design of the redundant acquisition system. The figure depicts two physical servers (hypervisors, depicted in gray boxes) each executing two virtual machines (VMs, represented in orange and light blue boxes). One VM is allocated for the acquisition of seismological data, while the other is responsible for data processing. The storage volumes for both VMs are situated within the storage array (green), which houses systems operating data and configurations ("/data") as well as the acquired seismological data ("/data acquisition"). The two independent systems run in parallel, executing identical tasks, with processed data from both workflows converging into synchronized instances of a unified database. Redundancy minimizes the risk of data loss – whether during maintenance procedures or due to system failures – and is thus essential for achieving fault tolerance, a critical requirement in microseismic monitoring. Additional off-site disaster recovery is based on a virtual machine located in a separate institutional data center in Rome (not represented in the Fig. 4).

This setup is mirrored on Hypervisor 2, identical in hardware and software, which hosts *Acquisition 2 VM* and *Processing & DB 2 VM*, identical to those on Hypervisor 1. The two pairs of virtual machines operate simultaneously and independently. If a machine in one pair stops, the other pair continues functioning, ensuring uninterrupted acquisition and processing of seismological data. This configuration allows for staggered maintenance and system updates without any interruption of service. Furthermore, both hypervisors connect to the storage array via two Ethernet cards configured in active-backup bonding [Bonding, https://wiki.debian.org/it/Bonding, last accessed on July 10, 2024], connected through two separate Netgear XS748T switches.

To meet the operational requirements of the monitoring system, we employ the SeisComP seismological software (Helmholtz Centre GFZ and Gempa, 2008; Hanka et al., 2010), widely adopted in the scientific community. SeisComP provides automatic and interactive multi-parametric data acquisition, quality control, analysis, processing, and data exchange, using standardized protocols and formats. Its functionalities include redundant acquisition processes, synchronized archives, dynamic network configuration based on automatic waveform quality parameters, optimized data protection where necessary, multi-parametric time series management, automated and interactive event detection and location, and an efficient data dissemination system. While we critically experiment with more sensitive detection methods, such as coherence analysis, machine learning, or template matching (Caredda et al., in preparation), we resolve to use automatic SeisComP modules because they are thoroughly tested and highly reliable, making them suitable for fiduciary monitoring. The same applies to the location methods used.

Modern seismic monitoring software systems must efficiently handle a variety of mission-critical tasks, including managing data transfer and acquisition, performing both automatic and supervised seismological analyses, and ensuring permanent, reliable data storage. Given this complexity, many institutions opt to use established, widely available software – whether commercial, proprietary, or open-source – rather than developing customized solutions, as implementing such a system requires considerable time and expertise. However, conducting direct comparative testing to evaluate specific benefits and limitations of each software option is generally impractical, so decisions are often based on prior knowledge and user experience. Several robust options exist in the field. The SEISAN package, designed for the interactive processing of seismic data across global, regional, and local scales (https://www.seisan.

info; Havskov and Ottemoller, 1999; Havskov et al., 2020), was originally developed for the Norwegian National Seismic Network in the early 1990s and has since grown with contributions from an active user community. Another widely used open-source package, Earthworm (http://www.earthwormcentral.org, Johnson et al., 1995), also benefits from community support for ongoing maintenance and expansion, although considerable customization is often required to adapt it to specific needs (e.g., Mele et al., 2010b). Antelope (https://brtt.com, Boulder Real Time Technologies, 2023), a commercial package, also provides comprehensive data archiving and analysis tools to manage seismic event workflows from acquisition to archiving, with additional user-contributed libraries available to address specific needs.

After assessing performance, reliability, and support requirements, we chose the SEISCOMP package (Hanka et al., 2010; Helmholtz Centre GFZ and GEMPA, 2008), which originated with the SeedLink real-time communication protocol for TCP/IP-connected networks in the GEOFON seismograph network. SEISCOMP allows consistent formatting of seismic time series from field data loggers to data centers, following the Standard for Exchange of Earthquake Data (SEED; see Ahern et al., 2009; Ringler and Evans, 2015) and data collection via SeedLink, a widely adopted protocol for seismic data transmission over TCP/IP (Helmholtz Centre GFZ and Gempa GmbH, 2008). Key metadata about the instrumentation is organized according to the FDSN StationXML Schema (Federation of Digital Seismograph Stations, 2022). Currently, our system manages a data stream of approximately 6 Gb/day, collected in real-time or near real-time from seven seismic monitoring networks, both public and private, comprising a total of 56 stations within the monitoring area.

Maintaining a continuous, real-time overview of the health of a seismic network is essential to guarantee a responsive earthquake monitoring system. Parameters such as latency, communication activity, power consumption, data completeness, and interference levels are monitored continuously. Additionally, monitoring noise levels at each site is crucial and is discussed further in the next section.

4. Background noise and disturbances

Figure 5 presents a flowchart outlining the essential workflow for setting up and executing routine data acquisition and analysis for the seismograph network. Each step is elaborated upon in the subsequent sections. Upon

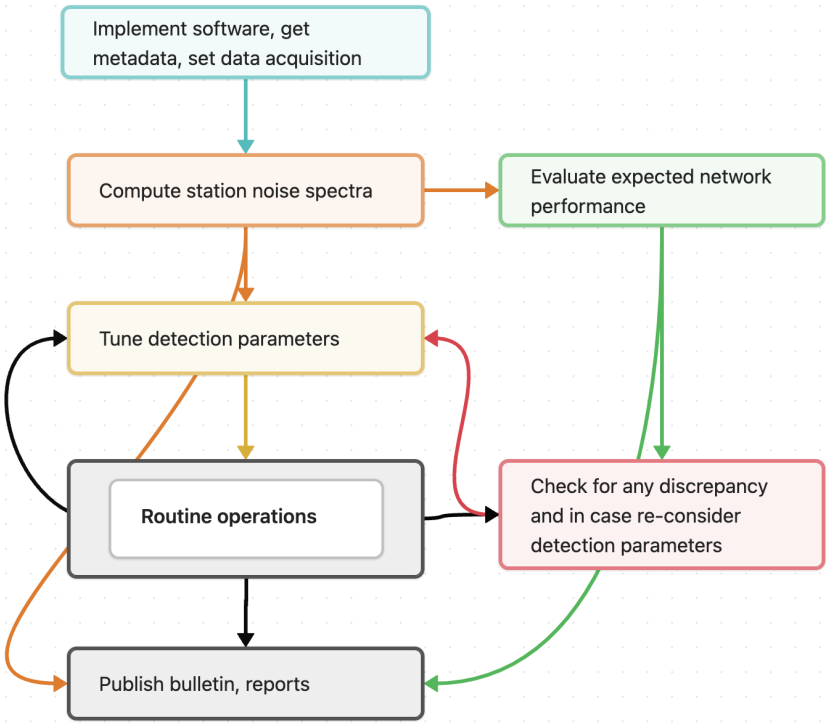

Figure 5. Workflow presenting the sequence of different steps as described in the text. Routine operations include quasi-real time supervision for atypical events as requested by the regulatory monitoring guidelines. Feedbacks are shown to indicate continuous re-analysis of detection parameters and monitoring of possible background noise variations

initiating the software, the primary and most crucial step involves analyzing background noise. It has long been recognized (for instance, Gutenberg, 1951) that seismometers record the uninterrupted motion of the ground caused by sources other than earthquakes. This component, collectively referred to as seismic noise, frequently obscures low-amplitude seismic records of earthquakes. Unlike stochastic internal electronic instrument noise, seismic noise is a deterministic process resulting from interactions between the fluid envelope and the solid Earth (Ardhuin et al., 2011). Historically, this phenomenon has often eluded the attention of seismologists. A notable example is the characteristic ground motion consistently recorded by seismometers worldwide, irrespective of any earthquake activity, within the period band between approximately 4 and 20 seconds, historically designated as "microseisms" (e.g., Berger et al., 2004). This ground motion originates from the interaction between systems of gravity waves in the ocean (e.g., Gualtieri et al., 2013, 2015). Background ground motion (outside earthquake-generated wave trains) in different period bands typically arises from distinct sources. For instance, atmospheric pressure fluctuations are responsible for ground motion with long periods, while anthropogenic sources or wind-generated motion accounts for short-period motion (Bormann and Wielandt, 2013; Smith and Tape, 2019; Quigley and West, 2023).

Recorded background seismic noise is typically evaluated using the Power Spectral Density (PSD; Peterson, 1993). The PSD represents an observable commonly employed to examine disturbances impacting station performance in distinguishing earthquake-generated signals from other sources, such as episodic cultural noise, variations in microseismic noise levels, and sensor malfunctions. The power spectral density of a continuous signal, predominantly composed of background noise, is computed for each individual time series after appropriate instrument response removal. Subsequently, these time series are averaged to generate a frequency plot representing the statistical probability density function. These probability densities are valuable in characterizing the performance of a seismic station and identifying potential operational issues (McNamara and Boaz, 2005). The probability density functions derived from the PSD identify the 'normal' ambient noise conditions with the highest probability, which may be considered stationary. Consequently, any deviation from these conditions can be detected as an anomaly, prompting appropriate intervention. We have implemented a quasi-real-time automatic procedure that nightly calculates the distribution of the PSD using the ObsPy routines (Beyreuther et al., 2010; Krischer et al., 2015) based on the direct Fourier method (Cooley and Tukey, 1965; McNamara and Buland, 2004). Figure 6 presents two such power spectral density probability density functions corresponding to the vertical component of two sample stations (IV.PTRP and VA.GRUE) with different noise signatures. Additionally, the plots include the New High (and Low) Noise Models (Peterson, 1993) for reference. The probability density has been calculated from the frequency of

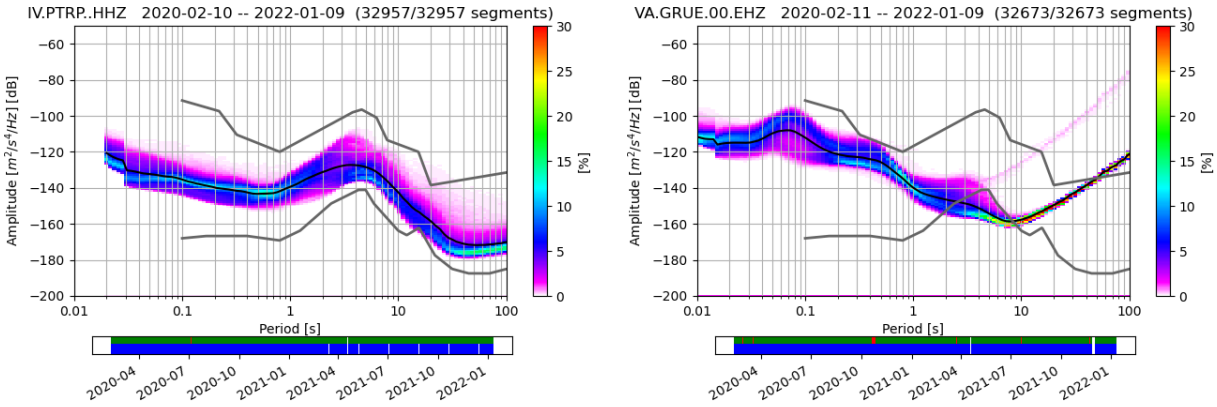

Figure 6. Probabilistic Power Spectral Density (PPSD – McNamara, 2004) plots for two stations of the CMS integrated network. The plot to the left refers to a seismic station installed outside urban areas; the right plot – with higher nose levels at short-period – is for a seismic station located inside the Val d'Agri basin and influenced by noise of anthropic origin. The black curves represent the high and low noise model limits (Peterson, 1993). Also note that the EHZ data stream of sensor 00 at site GRUE of network VA (identified by the string VA.GRUE.00.EHZ in the SEED convention) refers to a short-period, strong-motion sensor, that is not reliable for periods longer than ~1 s. This is shown by the too-low noise level, crossing the low noise model, due to reduced sensitivity in that period band. Also note that for periods T > 10 s the data only show the internal electronic noise of the sensor, that does not exhibit daily variation. In the bottom color scale, green patches represent available data, red patches are gaps in the data streams, and blue patches mark the data that contributed to the histogram.

measured spectral densities. The comparison reveals a quieter broadband station on the left, exhibiting noise levels that approach the minimum noise model limit. Station VA.GRUE exhibits a noisier periodicity at shorter intervals, potentially attributable to anthropogenic activities within that range. However, it exhibits a significant reduction in noise above the period of approximately 1 second. Notably, it does not conform to the well-known bump that reaches a maximum at around 5 seconds, which is attributed to ocean-generated microseisms. This is because the sensor is a short-period type, characterized by a narrow line that widens for periods exceeding 1 second. The internal electronic noise, which exhibits minimal fluctuation, is responsible for the increase in the line. Figure 7 presents a summary of the medians of probability density functions calculated for all stations and components, separately plotted for the monitoring region and sensor type (short-period and broadband velocity sensors). Additionally, the New High (NHNM) and New Low (NLNM) Noise Models (Peterson, 1993) are included for reference. At short periods (duration less than 1 second), the group of curves exhibits significant variability, with higher noise levels generally indicating the presence of ground motion caused by local industrial or anthropogenic activities. At periods longer

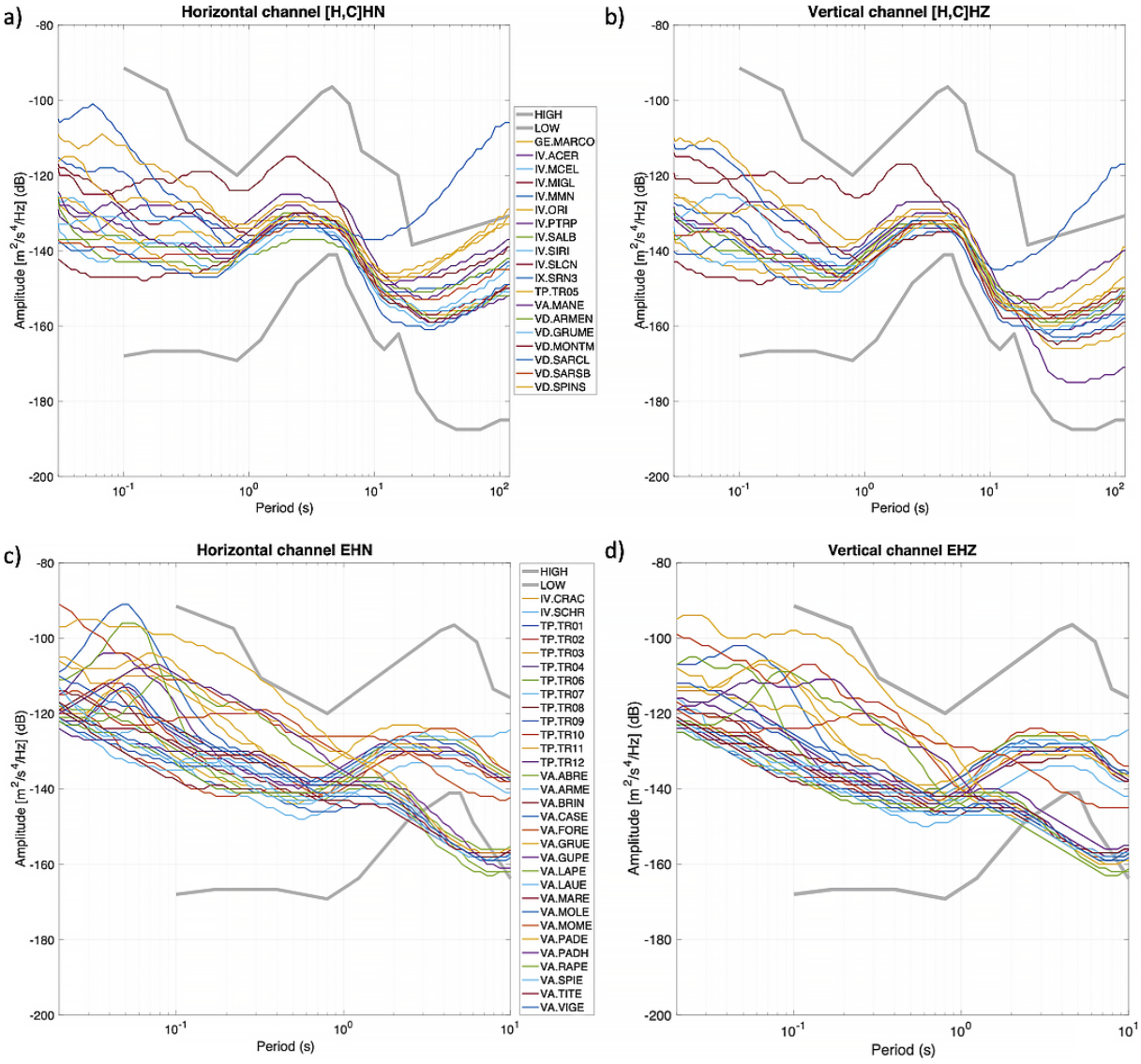

Figure 7. Median curves of the power spectral densities for the operating stations forming the integrated CMS seismic Network during the period from April 2020 to November 2021. Each line represents a single station, color coded according to the inset legend. The upper and lower light gray lines correspond respectively to the NHNM and NLNM models. (a) North-South horizontal component and (b) Vertical component of the broadband stations, (c) North-South horizontal component and (d) Vertical component of the short period stations (velocimeter). Channel naming follows the FDSN SEED convention (Ahern et al., 2009) by which the first letter H, C designates a broad band sensor sampled at high rate, while letter E identifies a short period sensor.

than 1 second, some of the 'short-period' sensors are unable to resolve true ground motion and only display internal electronic noise. This is evident from the fact that the noise median is below the lowest recognized ground motion noise NLNM. Such plots facilitate the identification of stations with better and worse noise characteristics.

Seismographs are highly sensitive instruments, making them susceptible to recording various non-arthquake-related vibrations. Consequently, they are vulnerable to several potential technical malfunctions that network operators should be cognizant of. Ringler et al. (2021) have identified several atypical signals resulting from different instrument failures that network operators should be aware of. These signals can often be recognized in the time series or in the noise power spectral density plots that we will discuss in more detail below. Instead, we present here some abnormal signals, identified as due to natural or anthropogenic disturbances, that may be quite common to observe and useful to identify.

Figure 8 presents amplitude spectra of signals recorded at designated stations, exhibiting distinct characteristics. Stations VA.ARME and VA.MOME exhibit pronounced peaks attributed to a wind power facility. VA.FORE, VA.GRUE, and VA.PADE, influenced by varying distances, demonstrate a peak at 3.5 Hz indicative of industrial pumping activity.

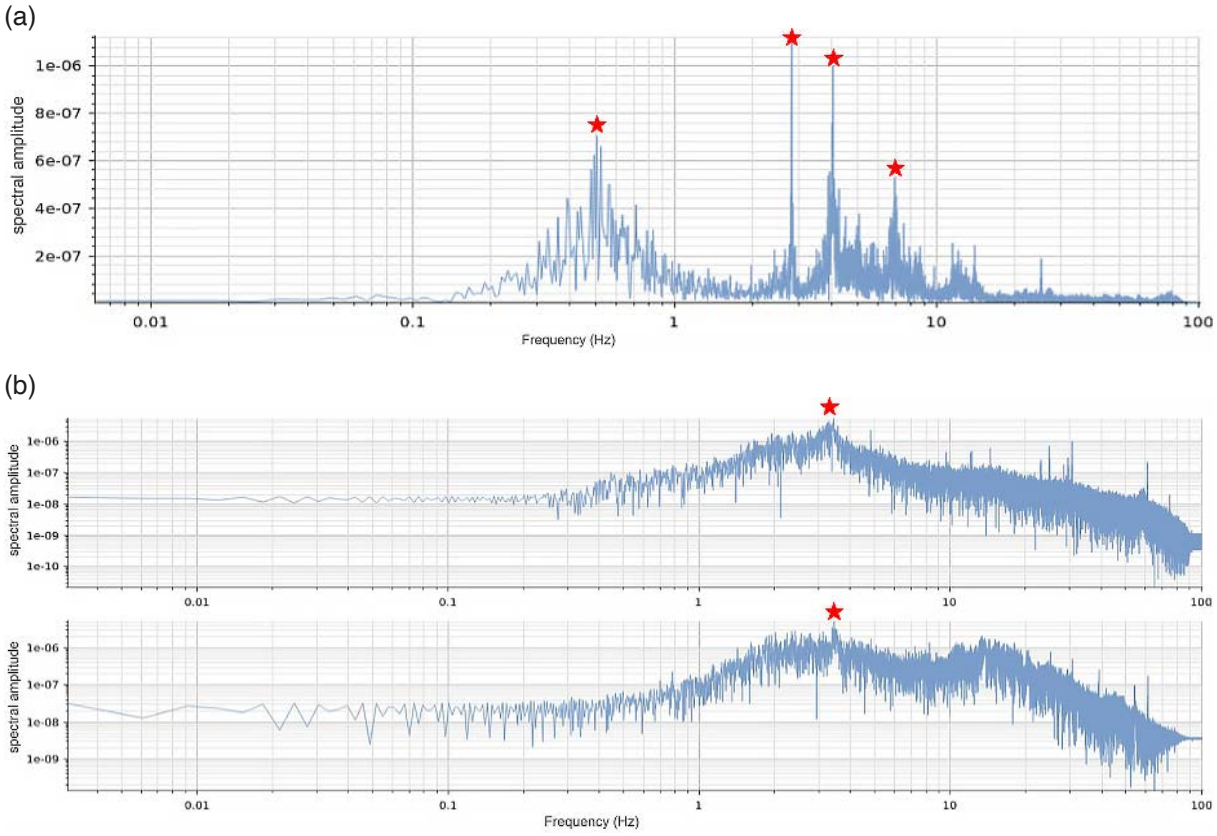

Figure 8. Sample amplitude spectra at selected stations: (a) broadband station ARME: the peak at 0.2-1.0 Hz is due to microseisms and is present at broadband stations; peaks at 2.8 Hz, 4 Hz, 7 Hz (all marked by a red star) are due to a nearby wind power plant; (b) short period stations FORE (top) and GRUE (bottom), showing a peak at ~3.5 Hz (vertical red dashed line) due to pumping activity, stronger at FORE that is closer; general high noise level at these stations is due to traffic. Note the presence of the broad peak due to microseisms (panel a, centered at ~0.4 Hz) that is attenuated at short period seismographs (panel b).

The presence of elevated noise levels can potentially obscure the records of seismograms. Figure 9 presents spectra for records of magnitude 2.2 (red) and 0.8 (green) earthquakes within the network, compared with background noise (black) at night (2 a.m.; left) and daytime (2 p.m.; right). Notably, daytime noise levels coincide with the signal of the M 0.8 earthquake, thereby obscuring its observation. Conversely, at nighttime, the earthquake's signal exceeds the noise. Seasonal noise variations, likely attributable to weather conditions, can also be observed.

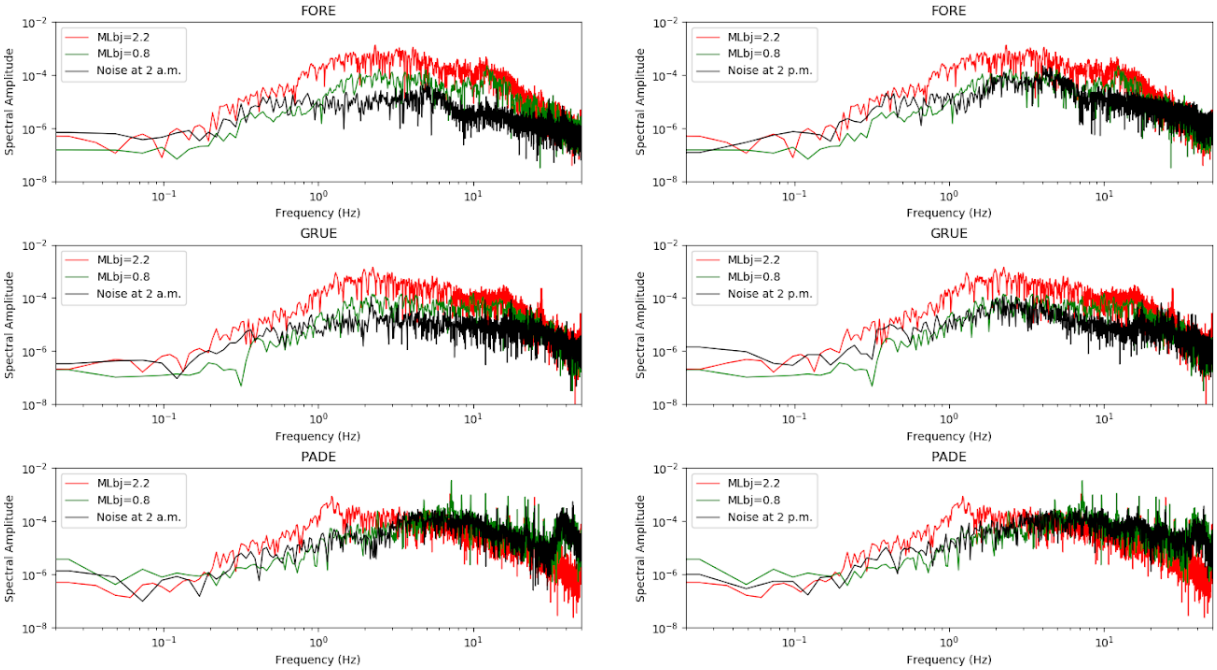

Figure 9. Comparison of signal from two earthquakes (MLbj = 2.2, red; MLbj = 0.8, green) with lower night-time noise level (left), and higher daytime noise (right) due to traffic, measured at different stations.

Station ORI (network IV) is situated in close proximity to the bell tower of Oriolo Calabro. As observed by Diaz (2020) and depicted in the plot of Fig. 10 (top), the seismograph registers chimes indicating every quarter of an hour. A closer examination of the bell tower signal, for instance, at approximately 04:43:25 UTC, reveals that the amplitudes and frequencies of the hourly chimes are significantly lower compared to those of the quarter-hourly intervals. A spectrogram is presented at the bottom of Fig. 10.

In addition to detecting explosions, continuous seismic monitoring may also record some unusual pulses that, at first glance, may be mistaken for earthquakes. For instance, the sonic boom of an airplane (as depicted in Fig. 11) can be recorded by seismometers. As is well-known, when an object, such as an aircraft, moves through the atmosphere at a speed exceeding the speed of sound in air, it generates a shock wave that couples with the ground and can be detected by seismometers (e.g., Kanamori et al., 1991). The pattern of arrival times may resemble that of a wavefront propagating from an earthquake epicenter. However, the ground isosurfaces can be shown to be hyperbolas (Kanamori et al., 1991), and the propagation speed of sound in air is significantly lower than that of body waves in the crust. Consequently, a valid solution for the source location cannot be obtained using a calculation optimized for earthquakes. Figure 11 presents an example of a sonic boom recorded by the local network on November 10, 2021, with impulsive amplitudes exceeding the noise level. Although the energy arrivals are clearly discernible, an attempt to attribute these arrivals to a seismic source fails. Such observations may remain a curiosity due to the limitations of a local network's aperture and the complexities of sound propagation in the atmosphere, which generally prevent the unique determination of altitude, speed, and source location, as demonstrated by Kanamori et al. (1991).

Ground motion caused by various natural and anthropogenic sources, such as wind, sea waves, thunderstorms, road traffic, machinery, and even bell towers, can fluctuate in amplitude but is always present and obscures the seismic signal. When ambient noise has a well-defined frequency signature (as exemplified by the sharp peaks in Fig. 8), it can be effectively removed by filtering the signal. However, in most cases, ambient noise simply contaminates the seismic signal, exacerbating the signal-to-noise ratio and impacting on network earthquake detection performance. Consequently, automatic detection parameters must be meticulously calibrated to account for the specific local characteristics. Although ambient noise fluctuates with time, sometimes regularly (e.g., nights are generally more quiet with less anthropic/industrial noise; summers are often quiet because of less wind and thunderstorms) we do not classify periods (e.g., quiet vs. noisy ones) and detection parameters do not vary with time.

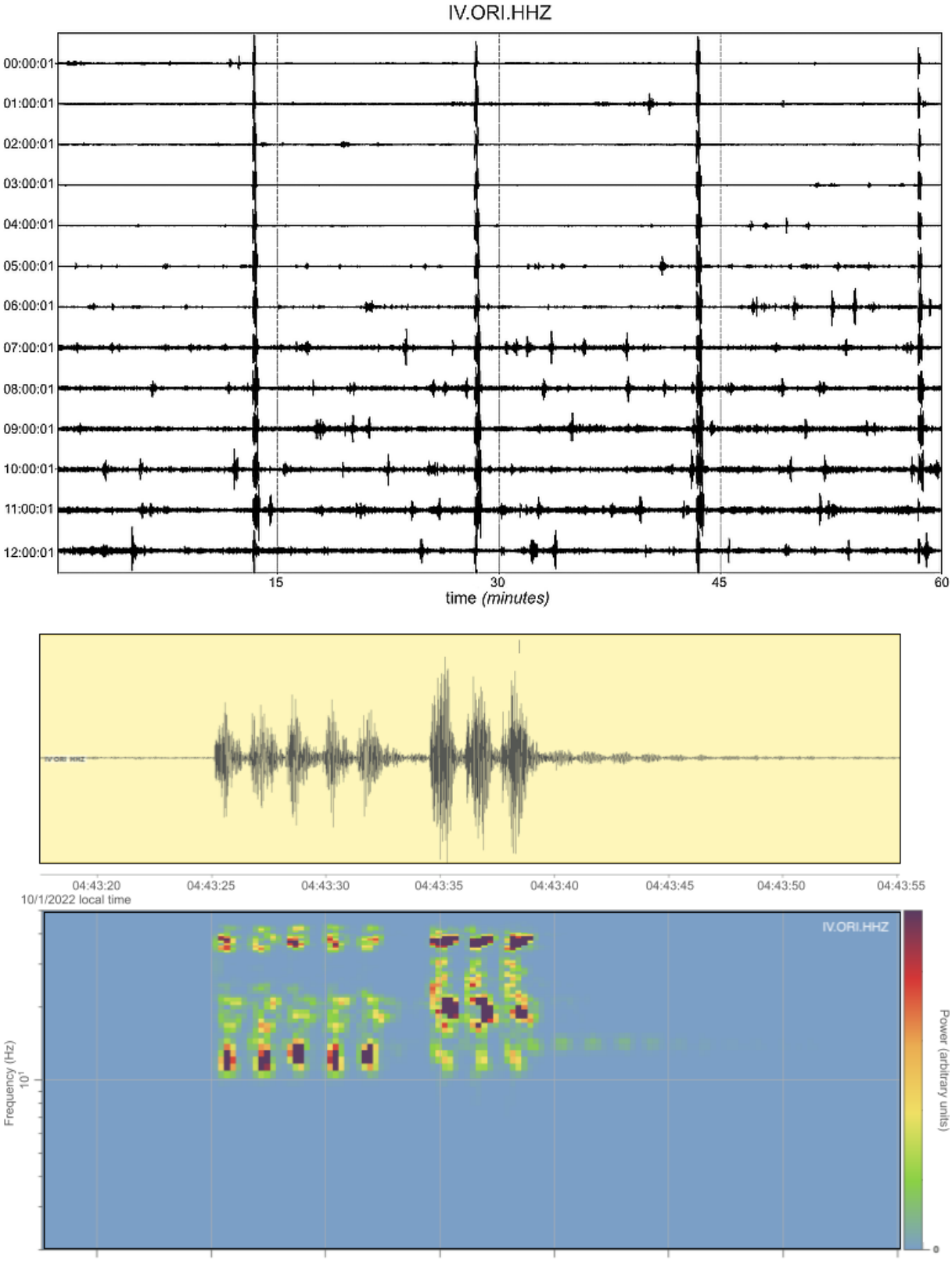

Figure 10. Chimes of the bell tower of Oriolo Calabro (CS) recorded by seismometer IV.ORI. The top figure shows regularity and clear alignment with time of the day (the clock is a few minutes early). The center seismogram, with its spectrogram (at bottom) shows the different signature of the hour and the 15′ bells: here the 04:45 time signal (slightly early) shows 4 1-hour chimes, followed by 3 quarter-hour chimes.

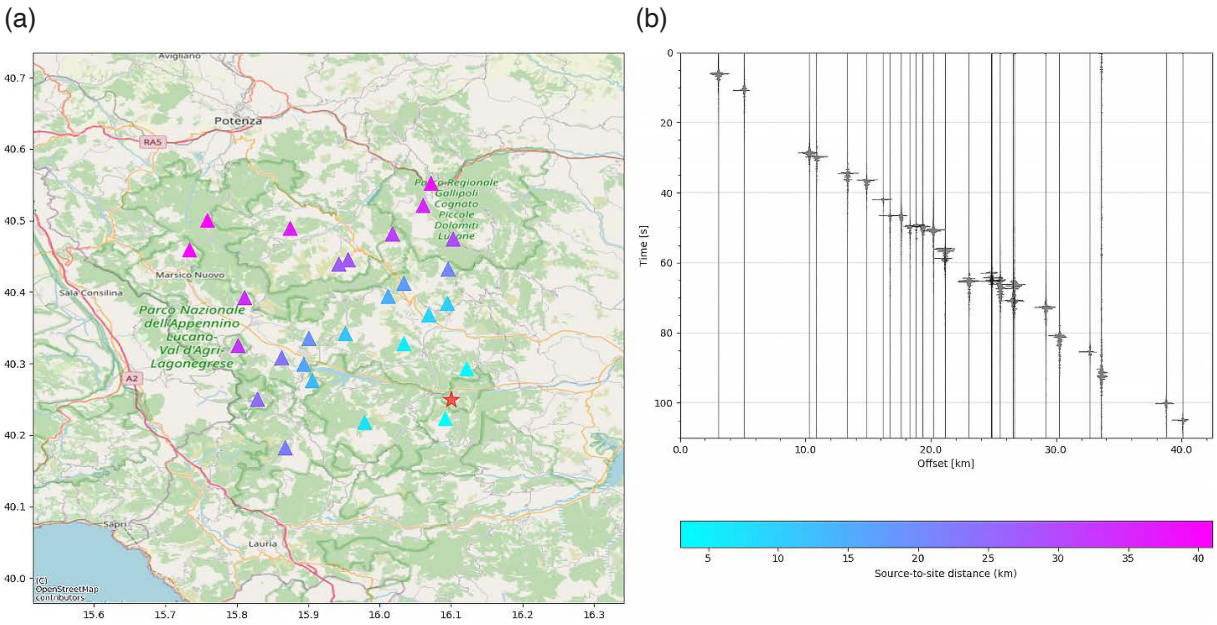

Figure 11. (a) Stations that recorded the sonic boom on 11/10/2021 (solid triangles) color coded following distance from the approximate source location (marked by a red star). (b) Seismograms showing energy arrivals sorted following distance from source.

5. Evaluation of network earthquake detection performance

We employ statistical analysis conducted on PSD data from various stations and components to calculate the theoretical performance of the entire seismic network in terms of detection threshold. This threshold represents the minimum magnitude event with a 90% probability of being identified and located using the data acquired by the network's stations (Ringdal, 1975). To estimate this network detection threshold, we adopt a mixed indirect approach. This approach involves comparing the noise level recorded at seismic stations with the theoretical spectra associated with rupture models for small earthquakes (McNamara et al., 2004; Marzorati and Bindi, 2006; Vassallo et al., 2012; Zaccarelli et al., 2021; Vassallo et al. 2023). We utilize the Brune source model in a homogeneous medium to compute the theoretical P and S amplitude spectra of ground velocity recorded at the actual distance of stations from a fixed hypocentral location. These amplitude spectra are subsequently compared with the actual noise spectra at each station to ascertain whether an earthquake of a specific magnitude could be detected and located at the stations. This process is repeated for all hypocenters within the volume and range of magnitude interest for the network. The circular fault model proposed by Brune (1970) provides a comprehensive description of both the near- and far-field spectra of earthquakes. In microseismic monitoring, it serves as a valuable tool for estimating the magnitude and frequency content of low-magnitude seismic events. The Brune model offers insightful information into the source spectrum, facilitating direct comparisons with the noise levels (PSD) recorded at monitoring stations. Furthermore, it establishes a crucial correlation between source spectral amplitudes and earthquake magnitudes, which is essential for determining detection thresholds. The Brune spectrum is computed after defining the seismic source and propagation medium parameters, including stress-drop ($\Delta\sigma = 2.0$ Mpa, Margheriti and Zollo, 2010; Vassallo et al., 2012), attenuation ($Q = 60$, Wcisło et al., 2017), P and S wave velocities ($v_P = 5{,}700$ m/s, $v_S = 3{,}000$ m/s), and density ($\rho = 2.6$ g/cm^3, Improta et al., 2017). Under these assumptions, the theoretical amplitude of P and S waves for a single station solely depends on the hypocentral distance, representing the earthquake's location.

To investigate the areal dependence of the detection threshold, we compute the source signal by exploring the hypocentral location along the nodes of a regular cubic grid with a cell size of $1 \times 1 \times 1$ km^3 within the investigated crustal volume. A regular grid was selected to guarantee that each point had an equal probability of becoming an earthquake epicenter. The horizontal cell size was determined based on the typical station spacing of 18 kilometers, with a few stations located 2 kilometers apart. Reducing the grid size was not feasible, as 88% of hypocentral locations have horizontal errors ranging from 0 to 1 kilometer. For each node, we then calculate the smallest amplitude associated with a seismic event recorded by at least five stations with a signal-to-noise ratio greater

than 5. From this amplitude value, we can retrieve the seismic moment that could have generated it. This moment magnitude (Mw) value is assumed to be the characteristic level associated with the smallest detectable event at the network. The 90th percentile curves in the 1-40 Hz frequency band for both vertical and horizontal components are utilized to compute the signal-to-noise ratio and determine the detection threshold map for P and S waves. The adopted percentile levels for the signal-to-noise ratio and threshold of station number for P and S detection ensure an accurate estimation of both location and magnitude, respectively (Vassallo et al., 2012). Figures 12a and 12b present the detection threshold maps determined for the joint network covering the Val d'Agri and Sauro Stream (Gorgoglione concession) valleys for P and S waves. These maps refer to a hypocentral depth of 5 km. This depth is a suitable compromise choice, considering the seismic activity of the region. The seismicity is characterized by numerous events within the range of 2 to 6 kilometers, with a relatively lower frequency of earthquakes distributed more evenly between depths of 6 and 13 kilometers (as depicted in Fig. 3). The smallest moment magnitudes detectable at all points within the Val d'Agri and Gorgoglione monitoring areas are 0.8 for P waves and 0.4 for S waves. However, the maps demonstrate significant spatial variations within the monitoring domains, with an average variation of approximately 0.2-0.3 units in Mw. This variation is attributed to the network geometry and the varying noise levels recorded by the different stations.

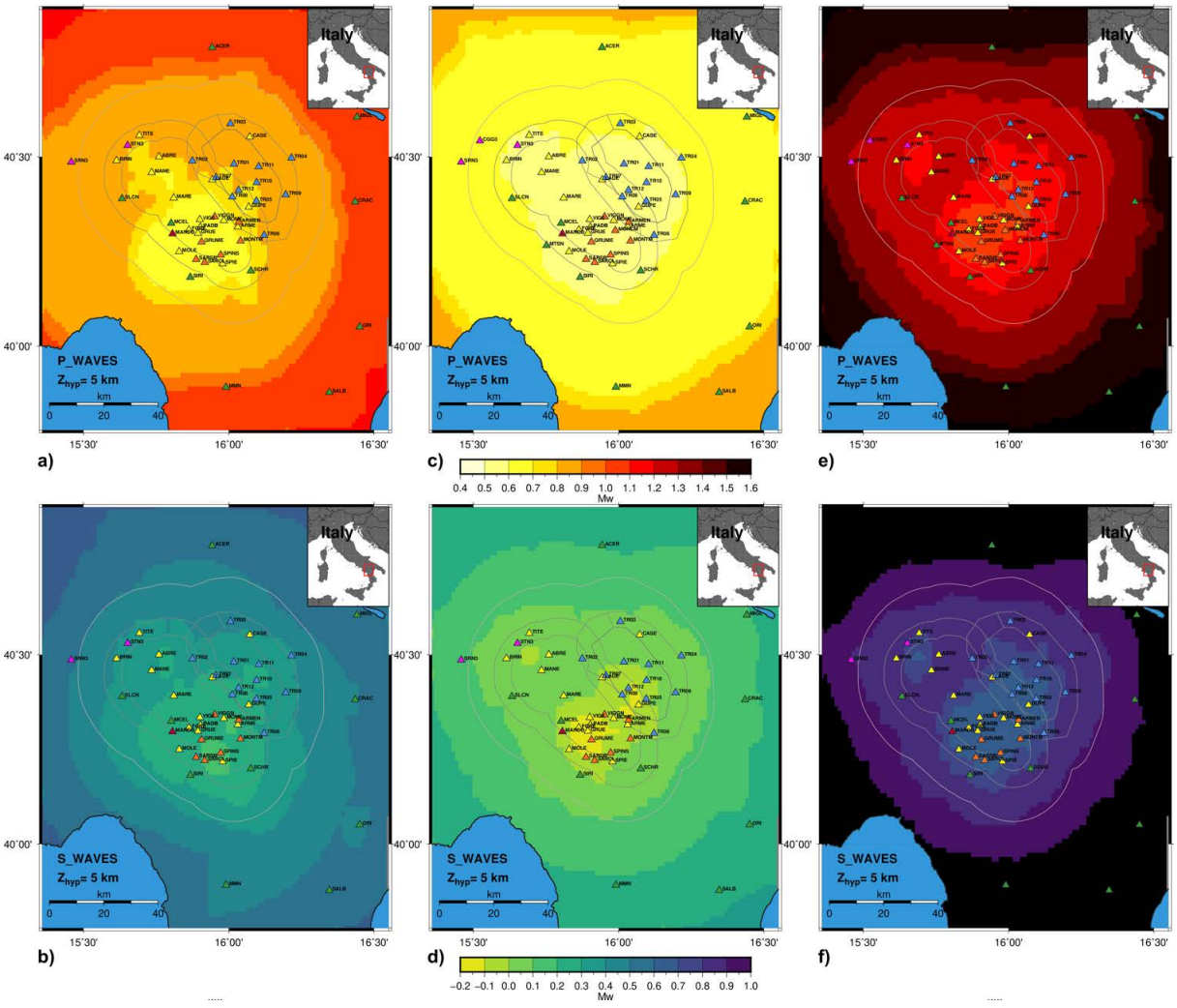

Figure 12. Detection threshold maps for the Val d'Agri and Gorgoglione areas: (a) and (b) are related to the P-waves and to S-waves, respectively by using the effective noise levels measured at the single stations of the different networks. In (c) and (d), the detection thresholds refer to the hypothetical case in which all stations would have the same noise level of MONTM, a station in the monitored area characterized by a low noise level. In (d) and (e) the maps are obtained by extending the noise levels of TR01 (a particularly noisy station) to all the stations used for the seismic monitoring of the area

In greater detail, the lowest detection magnitude is situated at the southernmost portion of the Val d'Agri (VA) concession, where the highest concentration of stations is located. Many of these stations, particularly those situated further west (such as MCEL, MARCO. MOLE, SIRI, SARSB, SARCL, SPINS, and SPIE), exhibit low noise levels on both vertical and horizontal components. Conversely, for the Grogoglione (TP) concession, the region with the lowest detection magnitude is the intersection of the VA and TP seismic networks. The higher density of stations in this area is the primary factor contributing to the reduction in detection thresholds compared to the remaining portions of the monitored concession.

To highlight the impact of spatial variations in seismic noise on the detection capabilities of networks, we present the detection thresholds for P and S waves that would be obtained if the noise levels at all stations were identical to those measured at MONTM (Figs. 12c and d). MONTM is a station characterized by relatively low noise levels. In contrast, the detection threshold is assumed to be the same as that of TR11 (Figs. 12e and f), which is characterized by a higher noise level compared to most other stations in the region. For the case of MONTM noise (Figs. 12c and d), the smallest magnitude detectable is 0.4 and 0.5 for P waves within the DI and DE domains (respectively; see Fig. 3 for definitions) for both VA and TP concessions. Conversely, for S waves, the smallest magnitude detectable is 0 within the DI and DE domains for both concessions. When using the noise characteristics of TR11 (Fig. 12e and f), the smallest magnitude detectable is 1.0 and 0.8 for P and S waves, respectively, within the DI and DE domains (see Fig. 3) for both VA and TP concessions. All these results are obtained with a reference hypocentral depth of 5 km, but the conclusions are generalizable to different depths of interest. Detection thresholds, intended as the smallest magnitude detectable at any point of the DI and DE of the concessions, are not significantly affected by the hypocentral depth (Supplementary Fig. S1). This is because detection thresholds are primarily influenced by the network's geometry and the noise levels recorded at the stations. In fact, within the depth range where the seismicity of the area is concentrated (in the first 12 km depth, Improta 2017), variations of approximately 0.21 in terms of detectable Mw are observed for some areas of concessions and for both P and S phases. However, in other areas of DI and DE, where station coverage is limited, variations in hypocenter depth do not affect the detection thresholds. The overall enhanced detection capability achieved through the integration of diverse seismic networks is illustrated in Supplementary Fig. S2.

6. Tuning automatic detection parameters

Adjusting parameters in the automatic modules of a real-time seismic monitoring system is crucial for enhancing its detection capabilities and minimizing false event detections. This tuning process requires consideration of specific network geometry and the noise characteristics of individual seismic stations. In our setup, real-time data acquisition and analysis are performed by SeisComP's automatic modules *scautopick* and *scanloc*, responsible for event detection and location, respectively. Key parameters for these modules include the *detect-filter* and *S-AIC* (Akaike Information Criterion, Küperkoch et al., 2010) for automatic picking, and *cluster-search*, *association*, and *score* for event location. To support optimal tuning, we conducted intensive offline analyses on representative datasets from our monitoring area. This approach first helped identify the system's most sensitive parameters and subsequently establish optimal values to enhance our network's capability to monitor local microseismicity effectively. Table 1 provides a comprehensive list of the most critical parameters, their default values, and the optimal values we have determined through an extensive trial-and-error process.

We refined the detection filters for P- and S-phase events, specifically targeting local seismicity to increase the number of automatic picks per event. Adjusting the S-AIC parameters (for S phases) notably contributed to detecting low-magnitude events, especially those near the network's perimeter (such as the Pertusillo seismic sequence to the southwest). By increasing the number of picks, we were able to refine the *score* value, representing the minimum number of P and S picks required to confirm an event, thereby balancing detected and false events. SeisComP's *S-AIC debugger* within the *scolv* module provided graphics-assisted tuning, helping us optimize pre- and detect-filters for S-phase picking.

Another critical aspect of enhancing network detection quality lies in associating picks generated by the detector with an origin. SeisComP employs a density-based spatial clustering method, DBSCAN (Ester et al., 1996), which relies on having a sufficient number of stations with spatially clustered picks within a defined real-time buffer to generate an origin. Given this method, it is essential to ensure accurate data acquisition timing. Because our network integrates data from multiple providers, acquisition delays of tens of seconds can occur, particularly with stations

Scautopick			
DetectFilter			
RMHP = 2	*ITAPER = 5*	*BW_HP = 3,3*	*STALTA = 0.1,5*
RMHP = 10	ITAPER = 30	BW = 4,4,20	STALTA = 0.1,5
DetectFilter (P phases)			
	ITAPER = 3	*BW_HP = 3,3*	
	ITAPER = 3	BW_HP = 3,3	
DetectFilter (S phases)			
		BW_HP = 3,3	
		BW = 4,4,15	
Scanloc			
MinScore = 6			
MinScore = 6			
Scevent			
MinimumDefiningPhases = 2			
MinimumDefiningPhases = 3			

Table 1. Detection parameters: default values, and final values as resulting from tuning. Scautopick, Scanloc, and Scevent are names of specific modules of SeisComP for, in turn: phase detection and picking; associate phase detections; and associate an origin to an event. RMHP: timespan to measure the running mean high-pass filter (seconds); ITAPER: timespan to apply the taper (seconds); BW: Butterworth filter, order, low frequency (Hz), high frequency (Hz); BW_HP: high-pass Butterworth filter, order and frequency (Hz); STA/LTA: length of the STA (seconds), length of the LTA (seconds); MinScore: score to be reached to send origin (there is a weight factor controlling the score associated to the origin and in particular P-phase score is 1 and S-phase score is 2); MinimumDefiningPhases: minimum number of picks for an origin that is automatic and cannot be associated with an event, to be allowed to form a new event.

receiving data through public data services rather than directly from the provider. These delays can result in missed small-event detections in specific monitoring areas, as delayed picks are discarded and cannot contribute to the cluster. Therefore, synchronizing timing across all network stations is essential. A teleseismic event, for instance, can serve as a reference signal for phase synchronization among receiving stations, ensuring timing alignment across providers. By comparing real-time and offline analysis results, discrepancies can highlight timing issues that real-time data temporization might miss.

With the software update addressing this issue, SeisComP's *scanloc* clustering module now bypasses temporal dependencies in real-time cluster creation. Overall, fine-tuning the automatic system parameters has enabled us to achieve an effective balance between detected and false events, optimizing our seismic monitoring capabilities.

7. Hypocentral location and seismic velocity models

Earthquake hypocenter location from recorded seismograms relies on accurate calculation of the travel time of seismic waves from the hypocenter to the seismographs. Therefore, reliable hypocentral location is contingent upon the seismic velocity model, which represents the wave speed used in these calculations (e.g., Bormann, 2012). The velocities of different wave types (P- and S-waves) vary significantly across geological structures, creating a complex three-dimensional speed field with sharp interfaces that is typically not well-constrained. This uncertainty in the velocity field limits the precision of computed travel times, which often falls short of matching the potential precision of time picks on seismograms, typically around 0.01 seconds with optimal signal-to-noise ratios. We explicitly address the sources of uncertainty in hypocenter determination in a subsequent section. However, we may point out here that using an appropriate seismic velocity model is crucial to minimize inaccuracies in hypocenter determination, justifying considerable efforts to acquiring one suited to the task (e.g., Kissling et al., 1994, and references therein).

In most cases, suitable velocity approximations are available in the form of a simplified, flat-layered 1D model, where wave speed is either constant or varies predictably (e.g., linearly) with depth within each layer. Body wave travel-time calculations are complicated by the dependency of wave paths on the velocity field, as described by the eikonal equation or, more simply, by Snell's law. Thus, any approximation of the velocity field also influences path determination, adding nonlinearity to the travel-time function concerning both hypocenter location and the wave speed field (e.g., Bormann, 2012). This is often addressed with iterative linearized inversion schemes, where the initial reference velocity model impacts the outcome. Selecting an appropriate reference velocity model is, therefore, essential (see, e.g., Kissling et al., 1994).

One widely-used approach for defining a reference velocity model involves computing a simplified 1D model that minimizes the travel-time residuals in a least-squares sense – often referred to as the *minimum model* (Kissling et al., 1994). However, this approach presents a challenge: accurately determining hypocentral locations ideally requires a known velocity field, yet solving for both Earth structure and hypocenters creates an under-determined inverse problem that necessitates assumptions or simplifications (Morelli and Dziewonski, 1991). A common solution is to first use a generic, a priori model (e.g., a regional model or one derived from geological data) to calculate preliminary hypocenter locations, which can then be refined using a local approximation. This iterative approach, relying on successive linearizations, is broadly accepted as a practical means of addressing the nonlinear nature of the location and velocity model inverse problem. The interdependence and trade-offs between hypocentral parameters and Earth heterogeneity have been explored by researchers such as Piromallo and Morelli (2001). For example, if inversion for a minimum model is intended, initial wave speed values can be sampled from a regional model, such as Molinari and Morelli's (2011) model for the European domain, which may be adequate for initial computations.

Although a dedicated inversion may be challenging due to the aforementioned difficulties, it may not be strictly necessary if a comprehensive literature review provides reliable local models. For our study area, several models are available (Valoroso et al., 2009; Improta et al., 2017; the regional mean model used by INGV for Italy's seismic monitoring system, Mele et al., 2010a, Scudero et al., 2021; the ENI operator model obtained through personal communication). We selected Improta et al. (2017) as the reference 1D model because it is the most recent release for the study area and because, among the available models, it was computed using the most extensive data set. However, prior to its routine use for earthquake location monitoring activities in the Val d'Agri region, we validated the model's stability. We randomly generate 200 alternate models, each with the same number of layers, by randomly perturbing the velocity of the layers of the model by Improta et al. (2017) with a perturbation of $dv = \pm 0.2$ km/s. The travel times of the local dataset were then utilized to invert for a new 1D velocity model using Velest (Kissling et al., 1994) employing each of the 200 perturbed profiles as an initial model. We observe that the newly inverted models exhibit significant similarity to the initial model, with the median output model not being substantially different from the initial model by Improta et al. (2017), as shown in Fig. 13. Furthermore, we attempt to reduce or increase the number of layers in the model by Improta et al. (2017) to assess the resolution capability of the same dataset. In both cases,

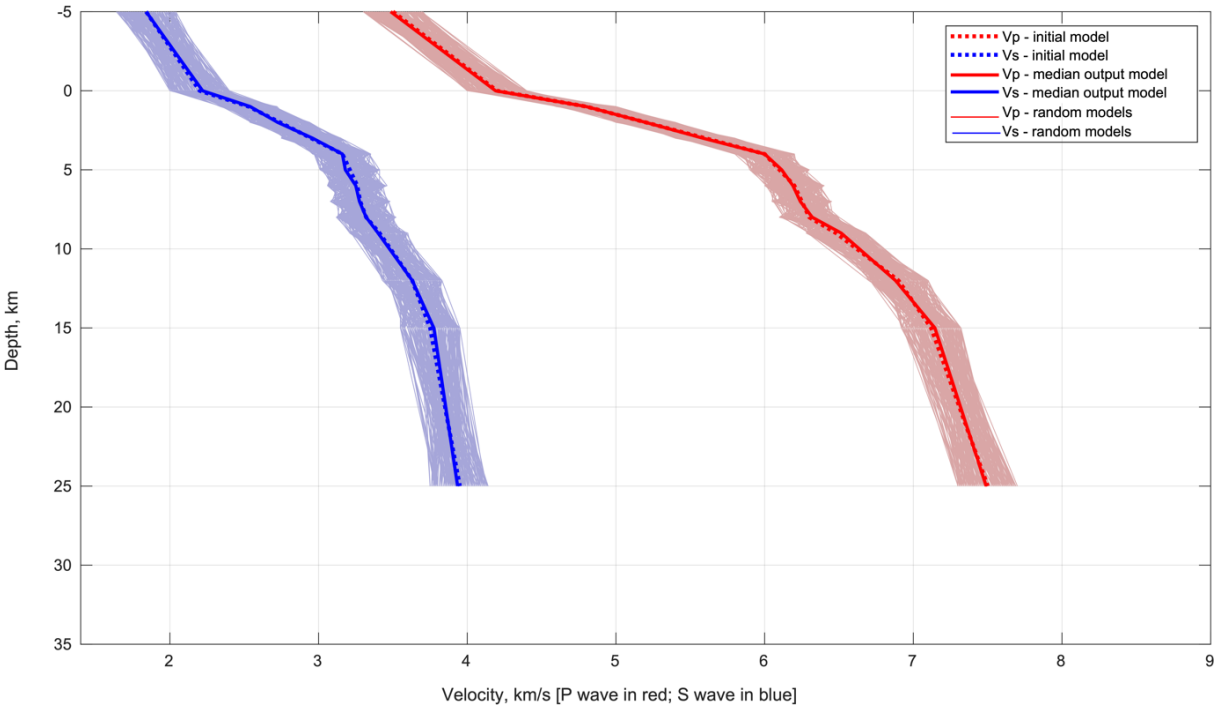

Figure 13. The vP, vS model by Improta et al. (2017) is shown (thick dashed lines, red for vP, blue for vS) together with the collection of newly inverted velocity profiles (thin continuous lines) obtained from slightly different initial models. The medians of such new inverted profiles, plotted with thick continuous lines, do not substantially differ from the starting model.

the solutions remain stable. Given the aforementioned results, we conclude that the existing data set is not able to resolve significant variations to the model by Improta et al. (2017), and select it as the most suitable 1D velocity model for routine data processing.

8. Magnitude determination

Richter (1935) observed that seismic amplitude, specifically the logarithm of maximum ground motion, recorded by a standard Wood-Anderson seismometer, systematically decreases with distance (Boore, 1989). To quantify earthquake size, he proposed calculating local magnitude (ML) relative to a reference event as:

$$ML = \log(A/A_0) = \log A - \log A_0 \quad (1)$$

where A and A_0 are the displacements of the earthquake and the reference event at the same distance (Richter, 1958). Richter established ML = 0 for a reference earthquake, setting A_0 to 0.001 mm at an epicentral distance of 100 km. Following this, Bakun and Joyner (1984) and Boore (1989) described that a magnitude-3 earthquake at 100 km would produce a peak amplitude of 1 mm on a Wood-Anderson seismometer. The amplitude (A) represents the maximum zero-to-peak amplitude, calculated as the geometric mean of the North (N) and East (E) horizontal components, using $A = \sqrt{(N^2 + E^2)}$ on a true or simulated Wood-Anderson seismograph. The term $(-\log A_0)$ is the calibration function, normalizing for distance-dependent geometric spreading and regional attenuation. This empirical distance correction varies with seismic wave propagation and local crustal structure, and many regional versions exist (e.g., see Table 2). As modern networks monitor microseismicity with stations closer to the source, the calibration function now often incorporates focal depth (Z), where epicentral distance D is replaced by hypocentral distance $R = \sqrt{(D^2 + Z^2)}$.

$M_L = \log A + 1.00 \log(R/100) + 0.00301(R - 100) + 3.0$	Bakun and Joyner, 1984; Central California
$M_L = \log A + 1.11 \log(R/100) + 0.00189 (R - 100) + 3.0$	Hutton and Boore et al., 1987; Southern California
$M_L = \log A + 1.11 \log R - 0.00095 R + 0.69$	Stange, 2006; Central Europe
$M_L = \log A + 1.749 \log(R/100) + 0.00160 (R - 100) + 2.9445$	Di Bona, 2016; Italy
$M_L = \log A + 1.79 \log D - 0.58$	Bobbio et al., 2010; Irpinia
$M_L = \log A + 1.11 \log(R) + 0.00189 R - 2.09$	IASPEI, 2012 (in [nm])

Table 2. Calibration functions as a function of distance (D < 100 km) for different M_L formulae proposed by different authors for the regions listed. Di Bona (2016) has proposed a specific calibration function for calculating the magnitude of seismic events occurring in the Italian national territory. However, to guarantee uniformity of reported M_L values in the earthquake bulletin, the Italian Seismic Network (INGV, 2005; ISIDe, 2007) has continued to use the formula by Hutton and Boore (1987) for the last 30 years (Battelli et al., 2013).

For microseismic monitoring, such as in industrial concessions, the Bakun and Joyner (1984) formula is commonly applied (e.g., Munich Geophysical Observatory, ENI in Val d'Agri). Italian national seismic network magnitudes may differ significantly from those by local networks due to calibration function limitations at small distances (Braun et al., 2018b). Since ILG offers no magnitude calculation recommendation and ENI has used Bakun and Joyner's method since 2002, we chose to maintain this approach, ensuring compatibility with ENI's reported ML values. To test local applicability, ENI also evaluated the Bobbio et al. (2010) formula, tailored for the Irpinia area, but found it generally produces lower ML values than Bakun and Joyner (1984). For future monitoring, calculating moment magnitude (MW), which provides a more physically meaningful measure, may be preferable over changing the ML formula.

Calculating ML for local events with modern 1 Hz velocity seismometers requires simulating a Wood-Anderson (WA) seismogram by (i) removing the short-period instrument response from recorded data and (ii) convolving with the WA displacement response (Seidl and Stammler, 1984). For low-magnitude events (ML < 1.0), this process may amplify long-period noise, especially on horizontal components, where noise may surpass S-wave amplitudes, necessitating high-pass filtering. The ML calculation requires preset parameters: high-pass (HP) filter frequency, minimum Signal-to-Noise Ratio (SNR), and the choice between mean or median ML from individual stations. We examined ML variability across several parameter choices for different earthquake magnitudes: HP filter frequencies [0.1, 0.5, 1, 1.5, 2, 2.5, 3, 5] Hz; SNR thresholds of 1.5, 2, and 3 (discarding waveforms with SNR below this value); and mean or median for final ML. Figure 14 presents an example showing how ML values vary by parameter choice: with a higher HP filter cutoff, magnitude decreases due to the removal of signal amplitudes, while a high SNR threshold can inflate magnitude estimates for low-energy events and lower HP cutoffs. We set the SNR default to 1 and identified the median as the most reliable estimate when data is sparse. Preferred HP cutoff frequencies were determined as: >0.5 Hz for ML ≥ 2, >1 Hz for 0 < ML < 2, and >1.5 Hz for ML < 0, thus ensuring signal integrity with minimal waveform modification. The SeisComp software provides an automatic initial estimate, upon which the HP filter is based.

9. Importance of addressing uncertainties

As any experimentally measured data, arrival time readings on seismograms are subject to random errors, primarily due to the presence of background seismic noise on the record, electronic jitter, or clock inaccuracy. These random errors contribute to the uncertainty of the final determination. After simplifying the underlying statistical model (typically approximated to a Gaussian probability density function for convenience), and making other assumptions, such as aleatoric uncertainty, is usually considered by common earthquake location programs,

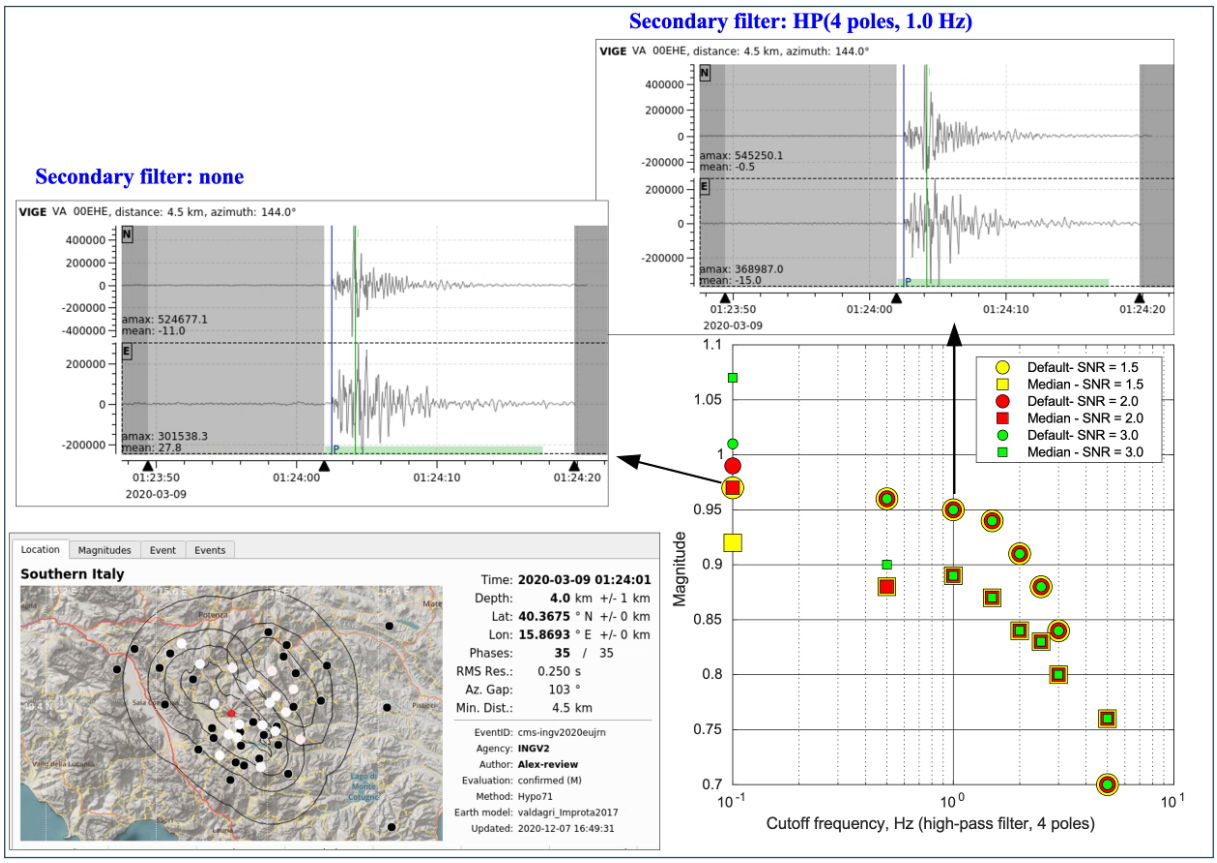

Figure 14. Comparison of different magnitude estimates for a sample event (red circle in map at bottom left), as a function of (i) frequency of high-pass filter cutoff; (ii) different values of the signal-to-noise ratio (SNR, different color of symbols, see legend); and (iii) measure of central location among individual station values (mean, default: round symbols; or median: squared symbols). Waveforms of station VIGE are shown for different filtering (the symbols for no filter should be out to the left of the plot and are plotted on the y axis).

such as HYPO71 (Lee and Lahr, 1972, 1975), HYPOELLIPSE (Lahr, 1984, 1999), or HYPOINVERSE (Klein, 1978, 2000), which compute a resulting (Gaussian) uncertainty of the hypocenter coordinates. In this process, these codes treat any discrepancy between observed and computed arrival times as random error. A more general approach is adopted by NonLinLoc (Lomax et al., 2000), which finds the complete, general, posterior probability density function and locates the maximum using a grid search.

Generally, however, the divergence between observed and calculated wave arrival times may also be attributed to other sources, which are epistemic in nature. In other words, they are a function of a systematic source of discrepancy, such as an incorrect account of the wave speed field in computing travel times. Piromallo and Morelli (2001) demonstrated the systematic effect of assuming a simplistic Earth model on hypocenter locations, mapping mislocation vectors with a scale of approximately 5 km in length. Consequently, when we select a specific Earth model for forward computations, we inevitably commit some systematic miscalculations, which have significant effects on the results. These effects may differ if we employ a different (legitimate) model. Earth structure is only one potential source of epistemic uncertainty; another significant source is represented by the various empirical ad-hoc rectifications implemented by location programs (such as HYPO71, HYPOELLIPSE, HYPOINVERSE, cited above, but many others as well) to mitigate bias caused by, for instance, irregular station azimuthal distributions or the possibility of outlier observations. Ultimately, different choices for the location code result in distinct hypocenters.

In their study published in 2020, Garcia-Aristizabal et al. identify four distinct sources of epistemic uncertainty in earthquake location determination. These sources include the location code and velocity model, the v_P/v_S ratio (often considered an independent parameter during inversion), and the operator's choice of arrival times. Each of these alternative options for the four sources of uncertainty is considered legitimate and well-considered wave speed models and location codes, as well as acceptable time picks.

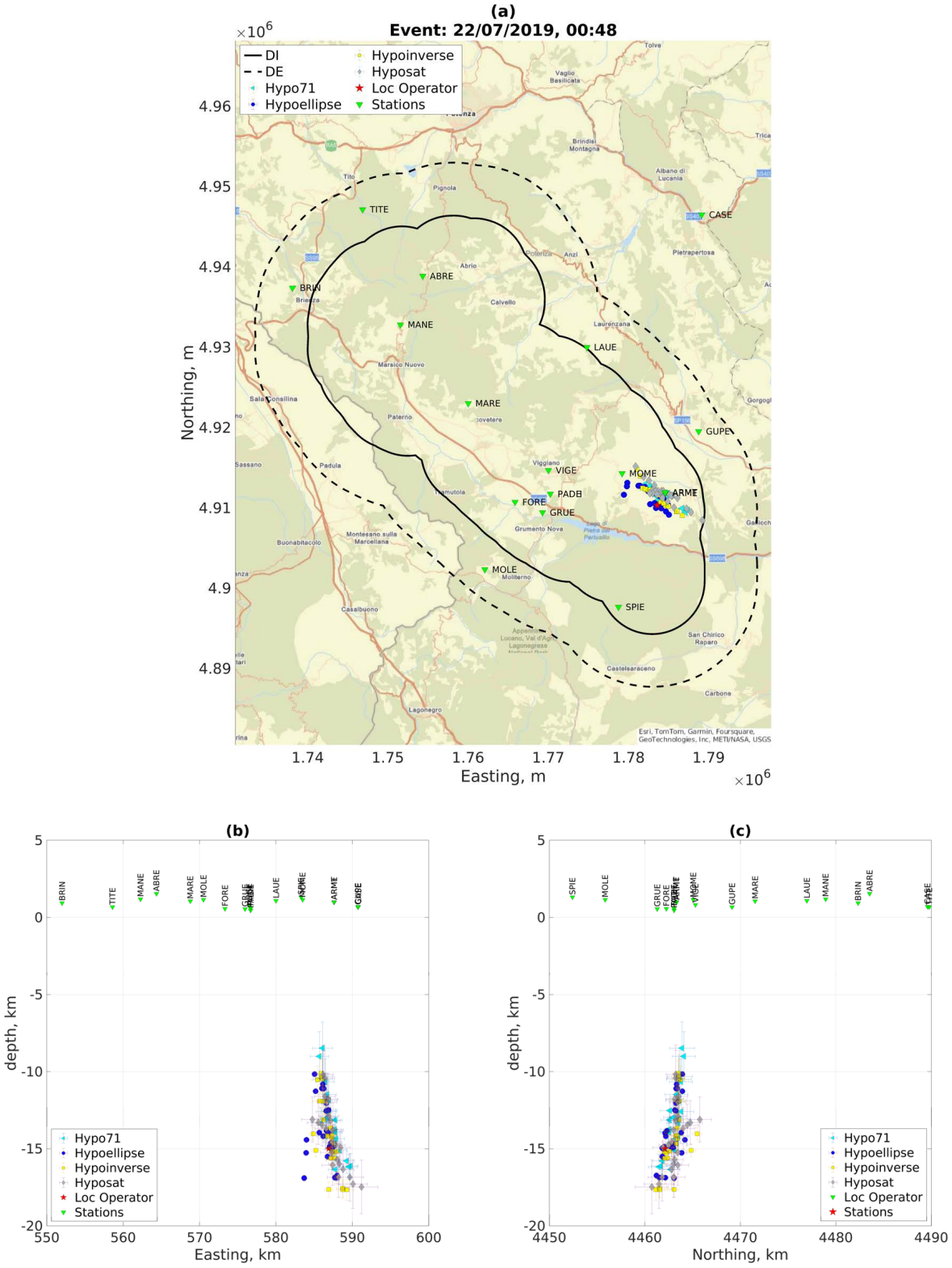

Figure 15. Set of hypocentral locations for the sample earthquake of 22 July 2019 (00:48 UTC). All the 96 solutions, resulting from the logic-tree based ensemble modeling based on different, legitimate, choices for operator, location code, wave speed model, and vP/vS ratio, are plotted with their error bars as blue symbols in: (a) map view; (b) and (c) vertical cross sections (after Garcia-Aristizabal et al., 2020). Seismic stations for network IV are plotted as inverted triangles and identified by station codes. Paths labeled as ID and ED delimit, in order, the Internal Domain and the Extended Domain – as defined by the guidelines by Dialuce et al., 2014 – for the Val d'Agri oil extraction concession.

Garcia-Aristizabal et al. then employ a logic-tree based ensemble modeling approach to address the impact of epistemic uncertainty resulting from the combination of 96 different legitimate choices. Figure 15 illustrates the resulting variability in the determination of the hypocenter for a sample earthquake. In their study published in 2020, Garcia-Aristizabal et al. identify four distinct sources of epistemic uncertainty in earthquake location determination using linearized inversion algorithms. The cloud of points, along with their formal error bars, demonstrates that epistemic uncertainty significantly exceeds the values resulting from aleatoric analysis (random pick errors).

Figure 15 presents the set of 96 plausible locations for a sample earthquake analyzed by Garcia-Aristizabal et al. (2020). These locations are situated on the boundaries of the Internal (ID) and Extended (ED) Domains of geophysical monitoring, as defined by the guidelines by Dialuce et al. (2014). These domains delineate the regions of alert for seismic events.

The figure illustrates that solutions derived from well-established models and procedures in the literature can distribute over a rather wide volume (see Garcia-Aristizabal et al., 2020, for further details). Acceptable solutions, arranged in a cloud-like configuration that differs significantly from a 3D Gaussian and not approximated by 'error bars' in geographical coordinates, are distributed to indicate whether they could trigger an alarm by occurring within or outside the critical internal domain. This example underscores the significance of assessing uncertainty, a desirable practice, particularly when the computational result may trigger responses for risk mitigation. In such cases, it is appropriate to explicitly consider the epistemic uncertainty associated with practical choices (e.g., location code, azimuthal weighting, wave speed model, arrival time picking approaches, etc.). These choices add uncertainty beyond that due to effects of random errors. We assert that when the outcome of an earthquake location process is employed to assess whether a predetermined threshold has been exceeded and could potentially have significant societal and industrial consequences (e.g., Dialuce et al., 2014), all known epistemic uncertainties should be taken into account in addition to the estimated aleatoric uncertainties. Consequently, any threshold exceedance should be communicated in a probabilistic manner rather than being presented as a binary Y/N value. Explicitly incorporating information on uncertainty, often in more complex forms than conventional 'error bars' on specific parameters, is crucial for effective communication about risks. The public's strong demand for information on potential effects of anthropogenic activities emphasizes the importance of accurately communicating the uncertainty surrounding certain processes. Communication strategies tailored for stakeholders and the general public are of paramount significance in geophysical monitoring of anthropogenic processes. However, these strategies are beyond the scope of this paper. Nevertheless, we emphasize the need for a comprehensive assessment of epistemic and aleatoric uncertainties in monitoring projects.

10. Discussion and conclusions

In contemporary seismology, establishing a fully automated, supervised, and real-time seismic acquisition and analysis system can be greatly facilitated by the accumulated multi-decadal experience of the scientific community. Additionally, the availability of suitable hardware and high-quality software is crucial. However, numerous significant decisions must be made, and the ultimate performance of the system depends on careful implementation, thorough comparison, and rigorous testing. Regardless of the specific scientific context motivating the installation and operation of an instrumental network for the study of microseismicity at a local scale, technical tools and performance are highly similar. Therefore, we believe that the general approach we describe is highly transposable to other similar applications. However, application to wider geographical scales may bring some substantial differences. Firstly, target earthquakes have larger magnitudes, and secondly, they are primarily recorded at longer distances. Consequently, the most important signal frequency band is lower than in local scale studies. This obviously generates differences in desirable instrumentation and in performing each of the steps of Fig. 5, although the general workflow largely remains the same.

Seismographs with broad response bands and high-resolution field data loggers equipped with highly accurate navigation satellite system (GNSS) timing capabilities, along with real-time data transmission, are readily available. Contemporary high-speed multiprocessor computers and high-capacity storage arrays effortlessly meet or surpass computational demands. Reliable and widespread standards for data and metadata (based on SEED definitions, Ahern et al., 2009; Ringler and Evans, 2015) coupled with highly recommended open data policies facilitate the seamless integration of data from diverse hardware into the workflow. Integration of various equipment becomes particularly advantageous in scenarios like ours (see Fig. 3), where open-access stations from other

networks are present in the region. Thanks to open data policies and the standardization of data formats (SEED) and protocols (SeedLink), analyzing an integrated, heterogeneous network does not necessitate a significantly increased computational effort; instead, it highly benefits from enhanced instrumental coverage. Advanced seismic network automatic data acquisition and analysis software packages are readily available, either as commercial or open-source software (e.g., SeisComP, https://www.seiscomp.de/; SEISAN, Havskov and Ottemoller, 1999; Earthworm, http://www.earthwormcentral.org; Antelope, https://brtt.com). Open-source codes are readily available for various purposes, including general data processing (e.g., ObsPy, Beyreuther et al., 2010; Krischer et al., 2015) and specifically for earthquake location (e.g., HYPO71, Lee and Lahr, 1972, 1975; HYPOELLIPSE, Lahr, 1984, 1999; HYPOINVERSE, Klein, 1978, 2000; NonLinLoc, Lomax et al., 2000). While the extensive accessibility of these codes may instill a sense of confidence, it is crucial to recognize that no code should be regarded as a "black box." Users should thoroughly examine user manuals and accompanying literature to gain a comprehensive understanding of the underlying principles that govern these codes.

We also wish to emphasize the paramount significance of selecting an appropriate model for seismic wave speeds, denoted as v_P and v_S. Available local models may exhibit considerable variability, particularly when they provide simplified descriptions (e.g., 1D profiles of heterogeneous crustal structures as a function of depth, limited to specific geographical averages). Such variability in local models can significantly contribute to epistemic uncertainty regarding the hypocentral locations, as demonstrated in a previous section. If hypocentral locations and their associated confidence levels are crucial outputs of the microseismic network, such as in geophysical monitoring of potentially induced seismicity, where hypocentral depth can influence hazard mitigation procedures (e.g., Dialuce et al., 2014), or serve as an indication of the causative process (e.g., Smith et al., 2020), an extensive assessment of location uncertainties, as outlined above, is imperative. Furthermore, it may be pertinent to address the specific issue of obtaining adequate knowledge of crustal structure, potentially through local-scale tomographic inversions (which are beyond the scope of the present contribution). Additionally, the local conditions of each seismographic station (e.g., elevation, local geology, site response, and so on) must be appropriately accounted for. The variability of background seismic noise can severely compromise the detection sensitivity of the microseismic network, necessitating a proper selection of instrument sites in the field. This aspect, however, is outside the scope of this contribution and should be addressed based on actual performance measurements during operational activities.

Data availability statement. We thank operators of seismograph networks IV (Istituto Nazionale di Geofisica e Vulcanologia – INGV, 2005), VD (CNR IMAA Consiglio Nazionale delle Ricerche – Italy, 2019), IX (Irpinia Seismic Network – ISNet, 2005) and GE (GEOFON Data Centre, 1993). Their data can be accessed through the International Federation of Digital Seismograph Networks (https://www.fdsn.org/networks/ (last accessed on July 10, 2024). Data from networks VA (ENI SpA, 2001) and TP (TOTAL E&P Italia Spa, 2018) are not public, and should be requested to the operators.

Acknowledgements. Figures have been prepared using the Generic Mapping Tools (Wessel and Smith, 1998), the ObsPy toolkit (Beyreuther et al., 2010; Krischer et al., 2015); QGIS (Open-Source Geospatial Foundation Project, http://qgis.org); GIMP (GNU Manipulation Program, retrieved from http://www.gimp.org) and MATLAB (version 24.2.0, R2024.b, The MathWorks Inc., 2024). During the endeavor described here, some of the authors benefitted from financial support from Regione Basilicata and Regione Toscana. We acknowledge the use of ChatGPT (https://chat.openai.com/) to identify need for improvement in the writing style of selected text snippets. We thank Associate Editor, dr. Diana Latorre, and two anonymous referees for comments that have improved the paper.

References

Ahern, T., R. Casey, D. Barnes, R. Benson, T. Knight and C. Trabant (2009). Standard for the Exchange of Earthquake Data Manual (SEED) Reference Manual, Version 2.4 (Updated August 2012), https://www.fdsn.org/pdf/SEEDManual_V2.4.pdf (last accessed July 10, 2024).

Ahern, T. (1994). The FDSN Archive at the IRIS Data Management Center, Ann. Geophys., 37,5, doi:10.4401/ag-4202.

Anselmi M., G. Saccorotti, D. Piccinini, C. Giunchi et al. (2020). Microseismic assessment and fault characterization at the Sulcis (South-Western Sardinia) field laboratory, Int. J. Greenhouse Gas Control, 95, 102974, ISSN 1750-5836, doi:10.1016/j.ijggc.2020.102974.

Ardhuin, F., E. Stutzmann, M. Schimmel and A. Mangeney (2011). Ocean wave sources of seismic noise, J. Geophys. Res., 116, C9, C09004, doi: 10.1029/2011JC006952.

Baisch, S., C. Koch and A. Muntendam-Bos (2019). Traffic Light Systems: To What Extent Can Induced Seismicity Be Controlled?, Seismol. Res. Lett., 90, 1145-1154, doi:10.1785/0220180337.

Bakun, W. H. and W. B. Joyner (1984). The ML Scale in Central California. Bull. Seism. Soc. of Am., 75, 5, 1827-1843.

Battelli, P., L. Arcoraci, M. Berardi, C. Castellano et al. (2013). Bollettino Sismico Italiano 2010, Quad. Geofisica, 115, 49.

Berger, J., P. Davis and G. Ekström (2004). Ambient earth noise: a survey of the global seismographic network, J. Geophys. Res., 109, B11307, doi:10.1029/2004JB003408.

Bertello, F., R. Fantoni, R. Franciosi, V. Gatti et al. (2010). From thrust-and-fold belt to foreland: hydrocarbon occurrences in Italy, Geological Society, London, Petroleum Geology Conference, doi:10.1144/0070113.

Beyreuther, M., R. Barsch, L. Krischer, T. Megies et al. (2010). ObsPy: A Python Toolbox for Seismology, Seismol. Res. Lett., 81, 3, 530.

Bianchi, I., M. Anselmi, M. T. Apoloner, E. Qorbani et al. (2015). The installation campaign of 9 seismic stations around the KTB site to test anisotropy detection by the Receiver Function Technique, Adv. Geosci., 41, 11-23, doi:10.5194/adgeo-41-11-2015, 2015.

Bobbio, A., M. Vassallo, G. Festa, A. Orefice et al. (2010): Calcolo della Magnitudo. In: G. Iannaccone and A. Zollo: Metodi e Tecnologie per l'early warning sismico, 7, 185-210.

Bobbio, A., M. Vassallo and G. Festa (2009): Local Magnitude estimation for the Irpinia Seismic Network, Bull. Seism. Soc. Am.99, 2461-2470, doi:10.1785/0120080364.

Bommer, J. J., S. Oates, J. M. Cepeda, C. Lindholm et al. (2006). Control of hazard due to seismicity induced by a hot fractured rock geothermal project, Eng. Geol., 86, 287-306.

Boore, D. M. (1989). The Richter scale: its development and use for determining earthquake source parameters, Tectonophysics, 166, 1,14.

Bormann, P. (Ed.) (2012). New Manual of Seismological Observatory Practice (NMSOP-2), IASPEI, GFZ German Research Centre for Geosciences, Potsdam; http://nmsop.gfz-potsdam.de, doi:10.2312/GFZ.NMSOP-2.

Boschi, E. and A. Morelli (1994). The MEDNET Program, Ann. Geophys, 37, 5. doi:10.4401/ag-4197.

Boschi, E., D. Giardini and A. Morelli (1991). MEDNET: the very broad-band seismic network for the Mediterranean, Il Nuovo Cimento C, 14, 79-99, doi:10.1007/BF02509260.

Boulder Real Time Technologies (2023) last accessed on July 10, 2024, https://brtt.com.

Braun, T., S. Cesca, D. Kühn, A. Martirosian-Janssen et al. (2018a). Anthropogenic seismicity in Italy and its relation to tectonics: State of the art and perspectives, Anthropocene 21, 80-94, doi:10.1016/j.ancene.2018.02.001.

Braun, T., M. Caciagli, M. Carapezza, D. Famiani, A. Gattuso et al. (2018b). The seismic sequence of 30thmay-9th June 2016 in the geothermal site of Torre Alfina (Central Italy) and related variations in soil gas emissions, J. Volcanol. Geotherm. Res., 359, 21-36, doi:10.1016/j.jvolgeores.2018.06.005.

Braun, T., S. Danesi and A. Morelli (2020). Application of monitoring guidelines to induced seismicity in Italy, J. Seismol., 1, 1-14, doi:10.1007/s10950-019-09901-7.

Burrato, P. and G. Valensise (2008). Rise and fall of a hypothesized seismic gap: source complexity in the 16 December 1857, Southern Italy earthquake, Mw 7.0., Bull. Seism. Soc. Am., 98,1, 139-148.

Butler, R. (1994). The IRIS Global Seismographic Network, Ann. Geophys., 37, 5, doi:10.4401/ag-4199.

Butler, R. et al. (2004). The global seismographic network surpasses its design goal, Eos Trans. AGU, 85, 23, 225- 229, doi:10.1029/2004EO230001.

Casnedi, R. (1988). Fossa Bradanica: Origine, sedimentazione e Migrazione, Mem. Soc. Geolog. It., 41.

Cello, G., E. Tondi, L. Micarelli and L. Mattionix (2003). Active tectonics and earthquake sources in the epicentral area of the 1857 Basilicata earthquake, southern Italy. J. Geodyn.36, 37-50, 19.

Cesca, S. and F. Grigoli (2015). Full waveform seismological advances for microseismic monitoring, Adv. Geophys., 56, 169-228, doi:10.1016/bs.agph.2014.12.002.

Chen, Y. T., Q. D. Mu and G. W. Zhou (1994). The China Digital Seismograph Networ, Ann. Geophys., 37, 5, doi:10.4401/ag-4194.

Chiaraluce, L., L. Valoroso, M. Anselmi, S. Bagh et al. (2009). A decade of passive seismic monitoring experiments with local networks in four Italian regions, Tectonophysics, 476, 1-2, 2009, 85-98, ISSN 0040-1951, doi:10.1016/j.tecto.2009.02.013.

CNR IMAA Consiglio Nazionale delle Ricerche (Italy) (2019). High Agri Valley geophysical Observatory [Data set]. International Federation of Digital Seismograph Networks, doi:10.7914/SN/VD.

Cooley, J. W. and J. W. Tukey (1965). An algorithm for the machine calculation of complex Fourier series, Math. Comput., 19, 297-301.

Dahm, T., D. Becker, M. Bischoff et al. (2013). Recommendation for the discrimination of human-related and natural seismicity, J Seismol 17, 197-202, doi:10.1007/s10950-012-9295-6.

Diaz, J. (2020): Church bells and ground motions, J. Seis., doi:10.1007/s10950-020-09935-2.

Di Bona, M. (2016). A Local Magnitude Scale for Crustal Earthquakes in Italy, Bull. Seismol. Soc. of Am., 106, 1, 242-258, doi:10.1785/0120150155. http://istituto.ingv.it/images/collane-editoriali/quaderni-di-geofisica/quaderni-di-geofisica-2013/quaderno115.pdf.

Dialuce, G., C. Chiarabba, D. Di Bucci, C. Doglioni et al. (2014). Indirizzi e linee guida per il monitoraggio della sismicità, delle deformazioni del suolo e delle pressioni di poro nell'ambito delle attività antropiche, Roma, https://unmig.mite.gov.it/wp-content/uploads/2018/07/85_238.pdf (in English: https://unmig.mite.gov.it/wp-content/uploads/2018/07/151_238.pdf; last accessed July 10, 2024).

Dziewonski, A. M. (1994). The FDSN: history and objective, Ann. Geophys., 37, 5, doi:10.4401/ag-4191.

Dost, B. (1994). The ORFEUS Data Center, Ann. Geophys., 37, 5, doi:10.4401/ag-4198.

ENI SpA (2001). VAL D'AGRI NETWORK [Data set]. International Federation of Digital Seismograph Networks, doi:10.7914/SN/VA.

Ellsworth, W. (2013). Injection-induced earthquakes. Science 341 doi:10.1126/science.1225942.

Ester M., H.-P. Kriegel, J. Sander and X. Xu (1996). A density-based algorithm for discovering clusters in large spatial databases with noise. In: Simoudis, E., J. Han, U. Fayyad eds., Proceedings of the Second International Conference on Knowledge Discovery and Data Mining (KDD-96), AAAI Press. pp. 226-231. ISBN 1-57735-004-9.

Ester, M., H. P. Kriegel, J. Sander and X. Xu (1996). A density-based algorithm for discovering clusters in large spatial databases with noise. In kdd, 96, 34, 226-231.

Federation of Digital Seismograph Stations (2022). FDSN StationXML Schema, https://www.fdsn.org/xml/station/ (last accessed on July 10, 2024).

Garcia-Aristizabal, A., S. Danesi, T. Braun, M. Anselmi et al. (2020). Epistemic Uncertainties in Local Earthquake Locations and Implications for Managing Induced Seismicity, Bull. Seismol. Soc. Am., doi:10.1785/0120200100.

Gasperini, P. (2002). Local magnitude revaluation for recent Italian earthquakes (1981-1996), J. Seism. 6, 503-524.

GEOFON Data Centre (1993). GEOFON Seismic Network [Data set]. Deutsches GeoForschungsZentrum GFZ, doi:10.14470/TR560404.

Giano, S. I. (2011). Quaternary alluvial fan system of the Agri intermontane basin (southern Italy): tectonic and climate controls, Geol. Carpathica, 62, 1, 65-76.

Giocoli, A., T. A. Stabile, I. Adurno, A. Perrone et al. (2015). Geological and geophysical characterization of the southeastern side of the High Agri Valley (southern Apennines, Italy), Nat. Haz. Earth Sys., Sci., doi:10.5194/nhess-15-315-2015.

Goebel, T. H. W., E. Hauksson, F. Aminzadeh and J. P. Ampuero (2015). An objective method for the assessment of fluid injection-induced seismicity and application to tectonically active regions in central California, J. Geophys. Res., Solid Earth, 120, 7013-7032, doi:10.1002/2015jb011895.

Grigoli, F., S. Cesca, E. Priolo, A. P. Rinaldi et al. (2017): Current challenges in monitoring, discrimination, and management of induced seismicity related to underground industrial activities: A European perspective, Rev. Geophys., 55, 310-340, doi:10.1002/2016rg000542.

Grigoli, F., L. Scarabello, M. Böse, B. Weber et al. (2018). Pick- and waveform-based techniques for real-time detection of induced seismicity, Geophys. J. Int., 213, 2, 868-884, doi:10.1093/gji/ggy019.

Gualtieri, L., E. Stutzmann, Y. Capdeville, F. Ardhuin et al. (2013). Modelling secondary microseismic noise by normal mode summation, Geophys. J. Int., doi:10.1093/gji/ggt090.

Gualtieri, L., E. Stutzmann, Y. Capdeville, V. Farra et al. (2015). On the shaping factors of the secondary microseismic wavefield, Journal of Geophysical Research: Solid Earth, 120, 9, 6241-6262, doi:10.1002/2015JB012157.

Gutenberg, B. (1951). Observations and theory of microseisms, In T. S. Malone (Ed.), Compendium of meterology, 1303-1311. Boston, Mass: American Meteorological Society.

Hanka, W. and R. Kind (1994). "The GEOFON Program", Annals of Geophysics, 37(5). doi:10.4401/ag-4196.

Hanka, W., A. Heinloo and K.-H. Jackel (2000). Networked Seismographs: GEOFON Real-Time data Distribution, ORFEUS Electronic Newsletter, last accessed on July 10, 2024, at https://eri-ndc.eri.u-tokyo.ac.jp/OHP-sympo2/report/o2001016-tsq/o2001016.ps.gz.

Hanka, W., J. Saul, B. Weber, J. Becker et al. (2010). Real-time earthquake monitoring for tsunami warning in the Indian Ocean and beyond, Nat. Hazards Earth Syst. Sci., 10, 2611-2622, doi:10.5194/nhess-10-2611-2010.

Havskov, J. and L. Ottemoller (1999). SeisAn: Earthquake analysis software, Seismol. Res. Lett., 70, 532-534.

Havskov, J., P. Bormann and J. Schweitzer (2012). Information sheet IS 11.1: Seismic source location, Version 2, in: New Manual of Seismological Observatory Practice (NMSOP-2), Bormann P. (Editor), IASPEI, GFZ German Research Centre for Geosciences, Potsdam, Germany.

Havskov, J., P. H. Voss and L. Ottemöller (2020). Seismological Observatory Software: 30 Yr of SEISAN, Seismol. Res. Lett., 91, 3, 1846-1852, doi:10.1785/0220190313.

Helmholtz Centre Potsdam GFZ German Research Centre for Geosciences and GEMPA GmbH (2008). The SeisComP seismological software package. GFZ Data Services, doi:10.5880/GFZ.2.4.2020.003.

Hetényi, G., I. Molinari, J. Clinton et al. (2018). The AlpArray Seismic Network: A Large-Scale European Experiment to Image the Alpine, Orogen. Surv. Geophys., 39, 1009-1033, doi:10.1007/s10712-018-9472-4.

Hutton, L. K. and M. Boore (1987). The ML scale in southern California. Bull. Seism. Soc. Am. 77, 2074-2094.

Improta, L., S. Bagh, P. De Gori, L. Valoroso et al. (2017). Reservoir structure and wastewater-induced seismicity at the Val d'Agri Oilfield (Italy) shown by three-dimensional V p and V p = V s local earthquake tomography, J. Geophys. Res., 122, 11, 9050-9082, doi:10.1002/2017JB014725.

Irpinia Seismic Network (ISNet) (2005). https://www.fdsn.org/networks/detail/IX/ (last accessed on July 10, 2024).

ISIDe Working Group. (2007). Italian Seismological Instrumental and Parametric Database (ISIDe) (Version 1). Istituto Nazionale di Geofisica e Vulcanologia (INGV), doi:10.13127/ISIDE.

ISPRA (2025). Geological Map 1:1.000.000, Tectonics, Istituto Superiore per la Protezione e la Ricerca Ambientale, http://portalesgi.isprambiente.it/it/lista-servizi-wms/Geological%20Maps (last accessed January 29, 2025)

INGV, Istituto Nazionale di Geofisica e Vulcanologia (2005). Rete Sismica Nazionale (RSN). Istituto Nazionale di Geofisica e Vulcanologia (INGV), doi:10.13127/SD/X0FXnH7QfY.

ITHACA Working Group (2019). ITHACA (ITaly HAzard from CApable faulting), A database of active capable faults of the Italian territory. Version December 2019. ISPRA Geological Survey of Italy, http://sgi2.isprambiente.it/ithacaweb/Mappatura.aspx.

Jepsen, D. (1994). The Australian National Seismograph Network, Ann. Geophys., 37, 5, doi:10.4401/ag-4192.

Johnson, C. E., A. Bittenbinder, B. Bogaert, L. Dietz et al. (1995). Earthworm: A flexible approach to seismic network processing, Incorporated Research Institutions for Seismology (IRIS) Newsletter, 14, 2, 1-4.

Kanamori, H., J. Mori, D. L. Anderson and T. H. Heaton (1991). Seismic excitation by the space shuttle Columbia, Nature, 349, 781-782.

Karasözen, E. and B. Karasözen (2020). Earthquake location methods, Int. J. Geomath., 11, 13. doi:10.1007/s13137-020-00149-9.

Kissling, E., W. L. Ellsworth, D. Eberhart-Phillips and U. Kradolfer (1994). Initial reference models in local earthquake tomography, J. Geophys. Res., 99, 19635-19646.

Krischer, L., T. Megies, R. Barsch, M. Beyreuther et al. (2015). ObsPy: a bridge for seismology into the scientific Python ecosystem, Compu. Sci., Disco, 8, 014003, doi:10.1088/1749-4699/8/1/014003, 2015.

Küperkoch, L., T. Meier, J. Lee, W. Friederich and EGELADOS Working Group (2010). Automated determination of P-phase arrival times at regional and local distances using higher order statistics, Geophys. J. Int., 181, 2, 1159-1170. doi:10.1111/j.1365-246X.2010.04570.x.

Lee, W. H. K. and J. C. Lahr (1972). HYPO71: A computer program for determining hypocenter, magnitude, and first motion pattern of local earthquakes, U.S. Geol. Surv. Open-File Rept., 72-224, doi:10.3133/ofr72224.

Lee, W. H. K. and J. C. Lahr (1975). HYPO71: A computer program for determining hypocenter, magnitude, and first motion pattern of local earthquakes, U.S. Geol. Surv. Open-File Rept., 75-311, doi:10.3133/ofr75311.

López-Comino. J. Á., T. Braun, T. Dahm, S. Cesca and S. Danesi (2021). On the Source Parameters and Genesis of the 2017, Mw 4 Montesano Earthquake in the Outer Border of the Val d'Agri Oilfield (Italy), Front. Earth Sci., 8, 617794, doi:10.3389/feart.2020.617794.

Liu, R.-F., J-Ch. Gao, Y.-T. Chen, Z.-L. Wu et al. (2008). Construction and development of China digital seismological observation network, Acta Seismologica Sinica, 21, 535-541.

Lomax, A., J. Virieux, P. Volant and C. Berge-Thierry (2000). Probabilistic Earthquake Location in 3D and Layered Models. In: Thurber, C. H., N. Rabinowitz (eds), Advances in Seismic Event Location. Modern Approaches in Geophysics, vol 18. Springer, Dordrecht. doi:10.1007/978-94-015-9536-0_5.

Malinverno, A. and W. B. F. Ryan (1986). Extension in the Tyrrhenian Sea and shortening in the Apennines as result of arc migration driven by sinking of the lithosphere, Tectonics, 5, 2, 227- 245, doi:10.1029/TC005i002p00227.

Margheriti, L. and A. Zollo (2010). High-resolution multi-disciplinarymonitoring of active fault test-site areas in Italy, Final Report S5-DPC-INGV Project, http://dpc-s5.rm.ingv.it/en/S5.html (last accessed on July 10, 2024), 14 pp.

Margheriti, L., C. Nostro, O. Cocina, M. Castellano et al. (2021). Seismic Surveillance and Earthquake Monitoring in Italy, Seismol. Res. Lett., 92, 1659-1671, doi:10.1785/0220200380.

Marzorati, S. and D. Bindi (2006). Ambient noise levels in north central Italy, Geochem. Geophys. Geosyst., 7, Q09010, doi:10.1029/2006GC001256.

Maschio, L., L. Ferranti and P. Burrato (2005). Active extension in Val d'Agri area, Southern Apennines, Italy: implications for the geometry of the seismogenic belt, Geophys. J. Int., 162, 2, 591-609.

Mazzoli, S., S. Barkham, G. Cello, R. Gambini et al. (2001): Reconstruction of continental margin architecture deformed by the contraction of the Lagonegro Basin, southern Apennines, Italy, J. Geol. Soc., 158, 2, 309-319, doi:10.1144/jgs.158.2.309.

McNamara, D. E. and R. P. Buland (2004). Ambient Noise Levels in the Continental United States, Bull. Seism. Soc. Am., 94, 1517-1527.

McNamara, D. E. and R. I. Boaz (2005). Seismic Noise Analysis System Using Power Spectral Density Probability Density Functions: A Stand-Alone Software Package, USGS Open-File Report, 2005-1438, https://pubs.usgs.gov/of/2005/1438/pdf/OFR-1438.pdf (last accessed on July 10, 2024).

Mele, F., L. Arcoraci, P. Battelli, M. Berardi, M. Castellano et al. (2010a). Bollettino sismico Italiano 2008, Quad. Geofis., 85, 1-48, https://www.earth-prints.org/handle/2122/6159.

Mele, F., A. Bono, V. Lauciani, A. Mandiello, C. Marcocci et al. (2010b). Tuning an Earthworm Phase Picker: Some Considerations on the *Pick_ew* Parameters, Rapporti Tecnici INGV, 164, http://hdl.handle.net/2122/6160.

Menardi Noguera, A. and G. Rea (2000). Deep structure of the Campanian-Lucanian Arc, Southern Apennine, Italy, Tectonophysics, 324, 239-265.

Molinari, I. and A. Morelli (2011). EPcrust: A reference crustal model for the European Plate, Geophys. J. Int., 185, 352-364, doi:10.1111/j.1365-246X.2011.04940.x.

Morelli, A. and A. Dziewonski (1991). Joint determination of lateral heterogeneity and earthquake location, in: Glacial Isostasy, Sea-Level and Mantle Rheology, edited by R. Sabadini et al., 515-534, Kluwer Acad., Norwell, Mass.

Morelli, A. and A. Dziewonski (1993). Body wave traveltimes and a spherically symmetric P- and S-wave velocity model, Geophys. J. Int., 112, 178-194.

Morelli, A., L. Zaccarelli, A. Cavaliere and R. M. Azzara (2021). Normal Modes of a Medieval Tower Excited by Ambient Vibrations in an Urban Environment, Seismol. Res. Lett. 93, 315-327, doi:10.1785/0220210038.

Nolte, K. A., G. P. Tsoflias, Y. Holubnyak, J. Raney and D. Wreath (2022). Designing monitoring networks for local earthquakes, J. Geophys. Engin., 19, 75-84, doi:10.1093/jge/gxab075.

North, R. G. (1994). The Canadian National Seismograph Network, Ann. Geophys., 37, 5, doi:10.4401/ag-4193.

Oliver, J. and L. Murphy (1971). WWNSS: Seismology's Global Network of Observing Stations, Science, 174, 4006, 254-261, doi:10.1126/science.174.4006.254.

Olivieri, M. and J. Clinton (2012). An Almost Fair Comparison Between Earthworm and SeisComp3, Seismol. Res. Lett., 83, 4, 720-727, doi:10.1785/0220110111.

Peterson, J. (1993). Observations and Modeling of Seismic Background Noise, USGS Open-File Report 93-322, 94, doi:10.3133/ofr93322.

Piromallo, C. and A. Morelli (2001). Improving seismic location: an alternative to three-dimensional structural models, Pure Appl. Geophys., 158, 319-347.

Popek, G. J. and R. P. Goldberg (1974). Formal requirements for virtualizable third generation architectures, Communications of the ACM., 17, 7, 412-421.

Priolo, E., M. Romanelli, M. P. Plasencia Linares, M. Garbin et al. (2015). Seismic monitoring of an underground natural gas storage facility: The Collalto seismic network. Seismol. Res. Lett., 86, 109-123.

Quigley, C. A. and M. E. West (2023). The Seismic Record of Wind in Alaska, Bull. Seismol. Soc. Am., 114, 613-626, doi:10.1785/0120230097-.

Richter, C. F. (1935): An instrumental earthquake magnitude scale, Bull. Seism. Soc. Am., 25, 1-31.

Richter, C. F. (1958). Elementary Seismology, W. H. Freeman and Co., San Francisco, California, 768.
Ringler, A. T., and J. R. Evans (2015). A quick SEED tutorial, Seism. Res. Let., 86, 6, doi:10.1785/0220150043.
Ringler, A. T., D. B. Mason, G. Laske, T. Storm and M. Templeton (2021). Why Do My Squiggles Look Funny? A Gallery of Compromised Seismic Signals, Seismol. Res. Lett. 92, 3873-3886, doi:10.1785/ 0220210094.
Ringler, A. T., R. E. Anthony, R. C. Aster, C. J. Ammon et al. (2022). Achievements and prospects of global broadband seismographic networks after 30 years of continuous geophysical observations, Rev. Geophys., 60, e2021RG000749, doi:10.1029/2021RG000749.
Romanowicz, B., M. Cara, J. F. Fel and D. Rouland (1984). GEOSCOPE: A French initiative in long-period three-component global seismic networks, Eos Trans. AGU, 65, 42, 753- 753, doi:10.1029/EO065i042p00753-01.
Roult, G. and J. P. Montagner (1994). "The-GEOSCOPE Program", Ann. Geophys., 37, 5, doi:10.4401/ag-4195.
Rovida, A., M. Locati, R. Camassi, B. Lolli et al. (2022). Italian Parametric Earthquake Catalogue (CPTI15), version 4.0 [Data set], Istituto Nazionale di Geofisica e Vulcanologia (INGV), doi:10.13127/cpti/cpti15.4.
Rothé, J-P. (1981). Fifty years of history of the International Association of Seismology (1901-1951), Bull. Seism. Soc. Am., 71, 905-923.
Roy, C., A. Nowacki, X. Zhang, A. Curtis and B. Baptie (2021). Accounting for Natural Uncertainty Within Monitoring Systems for Induced Seismicity Based on Earthquake Magnitudes, Front. Earth Sci., 9, 634688, doi:10.3389/feart.2021.634688.
Schultz, R., G. C. Beroza and W. L. Ellsworth (2021). A strategy for choosing red light thresholds to manage hydraulic fracturing induced seismicity in North America, J. Geophys. Res.: Solid Earth, doi:10.1029/2021jb022340.
Scudero, S., C. Marcocci and A. D'Alessandro (2021). Insights on the Italian Seismic Network from location uncertainties, J. Seismol. 25, 1061-1076, doi:10.1007/s10950-021-10011-6.
Seidl, D. and W. Stammler (1984). Restoration of broad-band seismograms (Part I), J. Geophys. 54, 114-122.
Serlenga, V. and T. A. Stabile (2019). How do Local Earthquake Tomography and inverted dataset affect earthquake locations? The case study of High Agri Valley (Southern Italy), Geomat., Nat. Hazards Risk, 10, 1, 49-78, doi:10.1080/19475705.2018.1504124.
Shearer, P. M. (1994). Global seismic event detection using a matched filter on long-period seismograms, J. Geophys. Res., 99, B7, 13713-13725, doi:10.1029/94JB00498.
Shiner, P., A. Beccacini and S. Mazzoli (2004). Thin-skinned versus thick-skinned structural models for Apulian carbonate reservoirs; constraints from the Val d'Agri fields, S Apennines, Italy, Mar. Petroleum Geol., 121, 7, 805-827.
Smith, K. and C. Tape (2019). Seismic noise in central Alaska and influences from rivers, wind, and sedimentary basins, J. Geophys. Res. 124, 11,678-11,704, doi:10.1029/2019JB017695.
Smith, J. D., R. S. White, J.-P. Avouac and S. Bourne (2020). Probabilistic earthquake locations of induced seismicity in the Groningen region, the Netherlands, Geophys. J. Int. 222, 1, 507-516, doi:10.1093/gji/ggaa179.
Snieder, R. and E. Şafak (2006). Extracting the building response using seismic interferometry: Theory and application to the Millikan library in Pasadena, California, Bull. Seismol. Soc. Am. 96, 2, 586-598.
Stange, S. (2006). ML Determination for Local and Regional Events Using a Sparse Network in Southwestern Germany, J. Seismol., 10, 247-257, doi:10.1007/s10950-006-9010-6.
TOTAL E&P Italia Spa (2018), https://www.fdsn.org/networks/detail/TP/ (last accessed June 8, 2023).
Trnkoczy, A. (2002). Understanding and parameter setting of STA/LTA trigger algorithm, in: P. Bormann, ed., IASPEI new manual of seismological observatory practice: GeoForschungsZentrum, 119.
Valoroso, L., L. Improta, L. Chiaraluce, R. Di Stefano et al. (2009). Active faults and induced seismicity in the Val d'Agri area (Southern Apennines, Italy), Geophys. J. Int. 178, 488-502, doi:10.1111/j.1365-246X.2009.04166.x.
Vassallo, M., G. Festa and A. Bobbio (2012). Seismic Ambient Noise Analysis in Southern Italy. Bulletin of the Seismol. Soc. Am., 102, 2, 574-586, doi:10.1785/0120110018.
Vassallo, M., G. Cultrera, A. Esposito, A. Mercuri et al. (2024). Temporary Seismic Network in the Metropolitan Area of Rome (Italy): New Insight on an Urban Seismology Experiment, Seismol. Res. Lett., 95, 4, 2554-2569, doi:10.1785/0220230290.
Warpinski, N. (2009). Microseismic Monitoring: Inside and Out, J Pet Technol, 61, 80-85. doi:10.2118/118537-JPT.
Wessel, P. and W. H. F. Smith (1998). New improved version of the Generic Mapping Tools released, Eos T. AGU, 79, 579.
Wcisło, M., T. A. Stabile, L. Telesca and L. Eisner (2018). Variations of attenuation and VP/VS ratio in the vicinity of wastewater injection: A case study of Costa Molina 2 well (High Agri Valley, Italy), Geophysics, 83, B25-B31, doi:10.1190/geo2017-0123.1.

Wielandt, E. and J. M. Steim (1986). A digital very-broad-band seismograph. Ann. Geophys. Ser. B., 4, 3, 227-232.
Zaccarelli, L., M. Anselmi, M. Vassallo, I. Munafò, L. Faenza et al. (2021). Practical Issues in Monitoring a Hydrocarbon Cultivation Activity in Italy: The Pilot Project at the Cavone Oil Field, Front. Earth Sci., 9, doi:10.3389/feart.2021.685300.
Zhu, W. and G. C. Beroza (2019). PhaseNet: a deep-neural-network-based seismic arrival-time picking method, Geophys. J. Int., 216-1, 261-273, doi:10.1093/gji/ggy423.

***CORRESPONDING AUTHOR: Andrea MORELLI**,
Istituto Nazionale di Geofisica e Vulcanologia, Sezione di Bologna, Bologna, Italy
e-mail: andrea.morelli@ingv.it